Chapter 3

NEW METHOD FOR ESTIMATING WHITECAP COVERAGE

I feel the whitecaps beckoning me
With passion to join their dance.
I find my heart is in unison
With such harmony and stance.

Eileen Breedlove, *THE OCEAN IN ME*

This chapter is devoted to the first major goal of this study: development of a new method for estimating whitecap coverage, W, from satellite measurements. The following sections report on the physical concept, implementation, error analysis, results, and validation of the new method.

3.1 Method concept

The new method for estimating W relies on variations in ocean surface emission induced by the presence of whitecaps. Variations in whitecapping and ocean emissivity can be detected as variations in the brightness temperature of the sea surface at microwave frequencies (§2.5.4).

According to relation (2.5), a hypothetical smooth ocean surface with no whitecaps, with an ambient water temperature of $T_s \approx 293$ K (20 ^{o}C) and an emissivity of $e \approx 0.39$ measured at 3 kHz (Stewart, 1985), would have a brightness temperature $T_B = eT_s \approx 114$ K. In reality, the ocean surface is never completely smooth but is composed of smooth, rough, and foamy patches, each with its own emissivity. These different emissivities combine into a composite emission of the ocean surface analytically

expressed with two terms quantifying the emissions of foam-free and foam-covered water (Stogryn, 1972; Pandey and Kakar, 1982; Wentz, 1983; Swift, 1990):

$$e = e_w(1-W) + e_f W\ .$$

Here e_w and e_f are the emissivities of seawater and foam, respectively, and W is the fraction of the ocean surface covered with foamy whitecaps, i.e., the whitecap coverage. In foam-free areas, seawater emissivity, e_w, consists of the emissivity of smooth water surface, called specular emissivity, e_s, and a corrective term, De_r, accounting for changes of ocean specular emissivity due to surface roughness, i.e., $e_w = e_s + \Delta e_r$. The composite ocean surface emission becomes:

$$e = (e_s + \Delta e_r)(1-W) + e_f W \qquad (3.1)$$

According to (3.1), if the ocean surface is 100% foam covered (W = 1), $e \equiv e_f$. Then if the foamy water-air mixture has $T_s \approx 293$ K again, and the foam emissivity is close to 1, e.g., $e_f \approx 0.98$, the brightness temperature of the ocean surface would be $T_B = eT_s \equiv e_f T_s \approx 287$ °K. The two extreme cases estimated here, a smooth ocean with no whitecaps and an ocean fully covered with whitecaps, give a 170-K range of possible changes in T_B—a significant potential for accurate derivation of W, on which the new method is built. Solving (3.1) for W yields:

$$W = \frac{e - e_s - \Delta e_r}{e_f - e_s - \Delta e_r} \qquad (3.2)$$

The task now is to find appropriate ways of calculating the four emissivities in (3.2).

3.2 Method implementation

Implementing the method concept involves three aspects. Analytical expressions for evaluating the emissivities in (3.2) have to be derived or found from the literature. Data for the measured variables entering these expressions have to be located and obtained. Finally, the impact of errors of measured variables on the error of W estimation must be examined.

3.2.1 Analytical expressions

This section lists all the analytical expressions necessary to evaluate seawater emissivity, e, specular emissivity, e_s, foam emissivity, e_f , and emissivity due to roughness, Δe_r.

Seawater emissivity e

Satellite-measured brightness temperature, T_B, of the ocean surface is used to calculate the composite ocean emissivity, e. Brightness temperature, T_B, of the ocean surface registered by a microwave radiometer viewing the ocean from a satellite, is given by the radiative transfer equation (RTE) (Stewart, 1985; Swift, 1990):

$$T_B = etT_s + T_{BU} + (1-e)tT_{BD} + (1-e)t^2T_{CB} \qquad (3.3)$$

Here the first term gives the ocean surface emission, influenced by the atmospheric transmission, t. The second term gives the brightness temperature, T_{BU}, of the atmospheric radiation traveling upward through the atmospheric column. The third term is the portion of the atmospheric radiation with brightness temperature T_{BD} that propagates downward, reflects back to space from the ocean surface, $r = 1 - e$, and attenuates passing an atmosphere with t. The last term describes the portion of the cosmic background radiation with brightness temperature T_{CB}, which enters the

atmosphere, reaches the Earth, and reflects back to space from the earth surface, (1 - e); the attenuation of this radiation on its way down and up through the atmosphere is accounted for with t^2. A satellite sensor records all these contributions together, but only the first term in (3.3) carries information for W on the ocean surface. The remaining three terms represent contribution of the atmosphere, which could be so strong that it could mask the emission from the surface completely. Thus, the atmospheric interference needs to be removed, and the procedure of doing this constitutes the so-called atmospheric correction.

Solving the RTE (3.3) for e yields the ocean surface emission as it is at any given moment of measurement from a satellite:

$$e = \frac{T_B - T_{BU} - tT_{BD} - t^2 T_{CB}}{tT_s - tT_{BD} - t^2 T_{CB}} \tag{3.4}$$

All quantities in (3.4) could be either measured or analytically evaluated.

The cosmic background radiation is a residual radiation from the big bang penetrating the entire universe (Smoot and Scott, 2000). The known value of T_{CB} is probably the most precisely measured quantity in cosmology.

The Special Sensor Microwave Imager (SSM/I) delivers daily T_B values over the entire globe. These T_B values do not have atmospheric correction and contain information related to both ocean surface phenomena and atmospheric constituents. The subtraction of and the normalization with atmosphere-related terms in (3.4) perform the atmospheric correction so that e is the emission from the ocean surface only.

The Advanced Very High Resolution Radiometer (AVHRR) measures the sea surface temperature, T_s, daily.

Wentz (1997) derived approximate formulae for T_{BU}, T_{BD}, and t. The atmospheric radiation propagating upward and downward is expressed in terms of effective air temperatures, T_U and T_D:

$$\begin{aligned} T_{BU} &= (1-t)T_U \\ T_{BD} &= (1-t)T_D \end{aligned} \qquad (3.5).$$

T_U and T_D are highly correlated with columnar water vapor, V [mm], and the sea surface temperature, T_s [K]; least square regression to values from 42,195 radiosonde flights yielded:

$$\begin{aligned} T_D &= c_0 + c_1 V + c_2 V^2 + c_3 V^3 + c_4 V^4 + c_5 (T_s - T_V) \\ T_U &= T_D + c_6 + c_7 V \\ T_V &= 273.16 + c_8 V + c_9 V^{3.33} \qquad V \le 48 \\ T_V &= c_{10} \qquad V > 48 \end{aligned} \qquad (3.6)$$

Here c_i are regression coefficients, V is derived as a geophysical product from SSM/I-measured T_B, T_V represents water temperature typical for water vapor V. The term T_s–T_V in the first equation accounts for the fact that the effective air temperature is typically higher (lower) for the case of unusually warm (cold) water (Wentz, 1997).

The atmospheric transmittance, t, at microwave frequencies (1 to 100 GHz) has four principle components due to rain, cloud liquid water, molecular oxygen, and water vapor (Wilheit and Chang, 1980; Swift, 1990). Heavy rainfall with a rain rate of 25-150 mm h^{-1} is the worst problem in the microwave range (Swift, 1990), but the occurrence of heavy rain is rare. Clouds and light rain (0.25 mm h^{-1}) have a comparable effect on the detection of the surface signal: both are translucent at frequencies below 100 GHz, and transparent at frequencies < 4 GHz. Molecular oxygen has a strong

resonant line in 50-70 GHz region, and water vapor has a relatively weak line centered at 22 GHz. Though weak, on humid days the 22 GHz water vapor line could contribute about 100 K to the signal registered from a satellite sensor. On dry days, the only interference left at frequencies below 50 GHz is about 5 K due to radiation from the wing of the 60 GHz oxygen line.

Correction of the observations for the rain signal is a complex problem (Wilheit and Chang, 1980; Wentz, 1997). Thus, unless retrieving rain intensity is pursued, the transmittance of the *nonraining* atmosphere is usually modeled. Wentz (1997) expresses the atmospheric transmittance along the SSM/I viewing path as:

$$t = e^{-k \sec q} \tag{3.7a}$$

$$k = a_O + a_V + a_L \tag{3.7b}$$

where q is the incidence angle of SSM/I (the angle measured from the normal to the beam), and k is attenuation coefficient accounting for the effects of oxygen with absorption coefficient a_O, of water vapor with a_V, and of cloud liquid water with a_L. Again, using 42,195 radiosonde flight values for V, Wentz (1997) gives approximate expressions for each of these absorption coefficients:

$$a_O = \left(\frac{c_{11}}{T_D} \right)^{1.4} \tag{3.8}$$

$$a_V = c_{12} V + c_{13} V^2 \tag{3.9}$$

$$\begin{aligned} a_{L19} &= c_{14} a_{L37} \\ a_{L22} &= c_{15} a_{L37} \\ a_{L37} &= c_{16} \left[1 + c_{17} \left(T_L - 283 \right) \right] L \end{aligned} \tag{3.10}$$

where c_i are regression coefficients, cloud liquid water, L, is derived as a geophysical product from SSM/I-measured T_B analogously to V, and $T_L = (T_s + 273)/2$ is the mean temperature between the surface and the freezing level.

Equations (3.5-3.10) completely determine seawater emissivity, e, in (3.4). All known values and regression coefficients are listed in Appendix A.

Specular emissivity e_s

On the basis of Kirchoff's and conservation of energy laws (§2.5.3), the emissivity, e, of the sea surface can be determined knowing the reflectivity, r, (Droppleman, 1970; Stewart, 1985):

$$e_h = 1 - r_h$$
$$e_v = 1 - r_v$$

where the subscripts h and v denote horizontal and vertical polarizations of the radiation. The specular emissivity, e_s, in (3.2) can be determined analogously:

$$e_s = 1 - r_s \qquad (3.11).$$

The reflectivity, r, in general, and specular reflectivity, r_s, in particular, can be calculated with good accuracy using the Fresnel formula (Schanda, 1976; Stewart, 1985):

$$r_h = \frac{(p - \cos q)^2 + q^2}{(p + \cos q)^2 + q^2}$$
$$r_v = \frac{(e' \cos q - p)^2 + (e'' \cos q + q)^2}{(e' \cos q + p)^2 + (e'' \cos q + q)^2} \qquad (3.12)$$

where

$$p = \frac{1}{\sqrt{2}}\left\{\left[\left(e' - \sin^2 q\right)^2 + e''^2\right]^{1/2} + \left(e' - \sin^2 q\right)\right\}^{1/2}$$

$$q = \frac{1}{\sqrt{2}}\left\{\left[\left(e' - \sin^2 q\right)^2 + e''^2\right]^{1/2} - \left(e' - \sin^2 q\right)\right\}^{1/2} \tag{3.13}$$

Fresnel formulae show that r_s, hence e_s, depends on the real, e', and imaginary, e'', components of the dielectric constant of water given as $e = e' - ie''$ (Rosenkranz and Staelin, 1972), and the angle of incidence, $è$, which, in this case, is that of SSM/I. Therefore, to evaluate r_s and e_s, expressions for e' and e'' are necessary.

The Debye equation represents the dielectric constant of any material as (Debye, 1929; Rosenktanz and Staelin, 1972; Stewart, 1985; Maul, 1985):

$$e = e_\infty + \frac{e_s - e_\infty}{1 + (iwt)^{1-b}} - i\frac{s}{we_0}$$

where $ù = 2ðf_r$ is the frequency of the radiation in radians interacting with the material, f_r is the frequency in Hz, $å_\infty$ is the dielectric constant at infinite frequency, $å_s$ is the static dielectric constant, $ô$ is the relaxation time, $ó$ is the ionic conductivity of water, $â$ is an empirical constant, and $å_0$ is the permittivity of free space. Appendix B gives definitions of these quantities and briefly explains the role of each term in the Debye equation. Grouping the real and imaginary terms in the Debye equation and assuming $â = 0$ (Klein and Swift, 1977), the explicit forms of the real and imaginary components of $å$are:

$$e' = e_\infty + \frac{e_s - e_\infty}{1 + w^2 t^2}$$

$$e'' = \frac{wt\left(e_s - e_\infty\right)}{1 + w^2 t^2} + \frac{s}{we_0} \tag{3.14}.$$

Values for $å_\infty$, $å_0$, and $ó$ are available from the literature (Table A.1). Klein and Swift (1977) proposed empirical expressions for the static dielectric constant, $å_s$ (T_s, S),

$$
\begin{aligned}
e_s(T_s, S) &= e_s(T_s)\, a(S, T_s) \\
e_s(T_s) &= s_0 + s_1 T_s + s_2 T_s^{\,2} + s_3 T_s^{\,3} \\
a(S, T_s) &= a_0 + a_{st} S T_s + a_1 S + a_2 S^2 + a_3 S^3
\end{aligned}
\qquad (3.15),
$$

and relaxation time, $\hat{o}$ (T_s, S),

$$
\begin{aligned}
t(T_s, S) &= t(T_s)\, b(S, T_s) \\
t(T_s) &= t_0 + t_1 T_s + t_2 T_s^{\,2} + t_3 T_s^{\,3} \\
b(S, T_s) &= b_0 + b_{st} S T_s + b_1 S + b_2 S^2 + b_3 S^3
\end{aligned}
\qquad (3.16).
$$

Here s_i, a_i, t_i, and b_i, are regression coefficients (Table A.2). AVHRR-measured T_s can be used again as in the case of e. Data for water salinity, S, are available from World Ocean Atlas 1998 (WOA98) (Levitus, 1998). All calculations use the 19 GHz channel of SSM/I, thus f_r and $\grave{u}$ are known (Table A.1). The choice of this frequency is clarified in §3.2.2.

Rough sea emissivity De$_r$

Over foam-free areas of the ocean surface at low to moderate wind speeds (< 10 m s^{-1}), surface roughness is the major contributor to ocean surface emission and consequent changes of brightness temperature (Stogryn, 1972; Swift, 1990). Thus, changes due to surface roughness must be assessed. Two approaches to modeling the surface roughness effect have been cited in the literature.

The first approach models the effect of surface roughness by modifying the Fresnel reflectivity coefficients (3.12) as $r_{\mathrm{mod}} = r(1 - Corr)$, where the term *Corr* is an expression containing surface roughness spectrum described with three parameters (Wu and Fung, 1972). When compared with actual T_B measurements of rough sea (Hollinger, 1971), the T_B values predicted by this approach show significant improvement over the T_B values predicted by the specular surface model not accounting for the roughness (Wu and Fung, 1972).

The second approach, employed by (Pandey and Kakar, 1982), represents the surface roughness effect with empirical expressions fitted on the Hollinger (1971) data:

$$\Delta e_{rh} = \frac{U_{10}}{T_s}\left(h_0 + h_1 q^2\right)\sqrt{f_r}$$
$$\Delta e_{rv} = \frac{U_{10}}{T_s}\left(v_0 + v_1 \mathring{a}^{v_2 q}\right)\sqrt{f_r} \qquad (3.17).$$

Here h_i and v_i are coefficients (Table A.2); U_{10} values could be derived as a geophysical product from SSM/I-measured T_B analogously to V and L.

Though the Wu and Fung (1972) model is based on sound physical considerations, Hollinger's empirical expressions (3.17) are used in the new method to evaluate the correction of ocean surface emission due to surface roughness. The main argument for this choice is that Hollinger's model introduces less new variables than the Wu and Fung's model, which is of importance for the error of the new method estimations (§3.2.3). Moreover, Wu and Fung's model compares excellently with Hollinger's data on which (3.17) are based.

Foam emissivity e_f

In a microwave emissivity model of a foam-covered sea, Pandey and Kakar (1982) employed an analytical expression for foam emissivity, e_f (T_s, f_r, $\grave{e}$), derived by Stogryn (1972) on the basis of reported radiometric measurements on foam. Another approach is pursued in this study. The new method employs Fresnel formulae in the form of (3.11-3.13) to find the reflectivity of foam, r_f, and then the foam emissivity, e_f, using the dielectric constant of foam, $\mathring{a}$:

$$e_f = 1 - r_f \tag{3.18}$$

This approach not only introduces the necessary dependencies of e_f on *è* and f_r through the expressions for r_f and $\mathring{a}$, but also involves the specific features of foam as a medium via $\mathring{a}$.

The dielectric constant of foam, $\mathring{a}$, could be determined by two methods. The first method represents the foam dielectric constant as a linear combination of the dielectric constants of air and water. The second, and more often used, method treats foam as a porous material and gives the foam dielectric constant as (Troitsky, 1962; Droppleman, 1970; Wentz, 1974):

$$e_f = e\,\frac{2Qe - 2Q + 3}{3e - Qe + Q}, \tag{3.19}$$

where Q is the ratio of the amount of *water* to total amount of air-water mixture within a unit volume. A more informative quantity for foam is the void fraction, *á*, defined as the ratio of the amount of *air* to the total amount of air-water mixture in a unit volume; the higher the void fraction, the more air the foam contains. Both these quantities are simply related as $á = 1 - Q$. Plugging $e = e' - ie''$ in (3.19) and rearranging, the real and imaginary components of $\mathring{a}_f$ are:

$$\begin{aligned} e'_f &= F_D\left[\left(e'^2 + e''^2\right)F' + e'F_N\right] \\ e''_f &= F_D\left[\left(e'^2 + e''^2\right)F'' + e''F_N\right] \end{aligned} \tag{3.20a}$$

where

$$F_D = \frac{1}{(3e' - Qe' + Q)^2 + e''^2(3-Q)^2}$$

$$F_N = Q(4Qe' - 2Q + 3)$$

$$F' = 2Q(3-Q)e' + 9(1-Q) \qquad (3.20b).$$

$$F'' = 2Q(3-Q)e''$$

At the chosen value of the void fraction *á*, hence *Q*, each evaluation of e' and e'' with (3.14-3.16) yields an evaluation of e_f' and e_f'' with (3.20).

Though the choice of *á* may introduce some error, this approach has a stronger physical foundation than the empirical expressions Stogryn (1972) proposes. Values of foam emissivity, e_f, computed with both approaches differ significantly. The Stogryn (1972) expression gives e_f values from 0.54 to 0.62 over a range of T_s; these are much lower than expected from the theory, O(1). Over the same T_s range, the new method gives e_f from 0.91 to 0.94. Thus, (3.20) with an appropriate choice of *Q* could be used confidently to obtain the foam emissivity, e_f.

Void fraction choice

The choice of the void fraction value *á*, hence of *Q*, is not easy. In the span of the whitecap lifetime, from formation to complete decay, the amount of air within both parts of the whitecaps, underwater bubble clouds and superficial foamy patches, changes from *á* ≈ 100% to < 1% (Lamarre and Melville, 1991; Dahl and Jessup, 1995). Bubble bursting and generation of sea-salt aerosols, however, take place in the superficial part of the whitecaps only. Thus, for the new method purposes, the search for *á* value narrows to choosing a void fraction appropriate for the surface part of the whitecaps.

The surface part of the whitecaps could be considered as composed of multiple foam layers with thickness of order of 8-10 cm in newly formed whitecaps, a stage termed A-stage (Monahan, 1988; 1993), and as a single one-bubble layer with thickness of order of 1-10 mm when the whitecaps decay, B-stage, (Williams, 1969; Rosenkranz and Staelin, 1972; Whitlock and el., 1982). Generally, most of the radiation emitted by a medium originates from a surface layer called penetration (or skin) depth (Schanda, 1976). The penetration depth at 19 GHz is of the order of 0.5 mm (Plant, 1990), less than or at most commensurate with the thickness of a single foam layer. Therefore, despite the fact that in any real situation there is a distribution of foam thickness values, the emission of foam always originates from a layer within which the amount of air is close to 100%. This is a hint that the value of the chosen $\acute{a}$ should be high.

As the foam thickness decreases, the foam emissivity, e_f, also diminishes. Droppleman (1970) modeled the microwave emissivity of sea foam and showed that for $\acute{a}$ = 99% e_f is independent of the foam thickness, D, when it is greater than the wavelength of the radiation, l, ($D/l > 1$), and e_f decreases slowly for $D/l < 1$ down to $D/l \approx 0.25$. For lower $\acute{a}$, in the 95-99% range, the curve $e_f(D/l)$ behaves in a similar manner, only the decreasing trend at $D/l < 1$ is faster. Thus, a choice of $\acute{a}$ in the range 95-99% would account fairly well for both the high e_f of newly formed whitecaps and the e_f decrease as whitecaps decay. The choice for this study is $\acute{a}$ = 98%, i.e., Q = 2%.

According to the Droppleman (1970) model, with this choice, the computed $\mathring{q}$ and e_f at 19 GHz ($l \cong 1.6$ cm) would represent all situations having foam thickness $D \geq 5$ mm. Cases of foam thickness $D < 5$ mm (a single foam layer composed of bubble caps protruding less than 5 mm above the sea surface) would be missed, and this may

introduce some underestimation of W. But since the emissivity of thinner foam decreases, it is believed that this underestimation is not crucial and the new method will adequately evaluate the foam presence with Q = 2%.

Compared to the photo approach of *in situ* measurements, the new method will certainly evaluate more adequately the whitecap coverage because it will "feel" both the thick active whitecaps in their initial A-stage, and if not all at least most of the B-stage of decaying whitecaps. Meanwhile, the photograph-based expression (2.3) accounts for B-stage whitecaps only (Monahan, 1993).

3.2.2 Data

Expressions (3.4-3.17) require data for brightness temperature, T_B, water vapor, V, cloud liquid water, L, wind speed, U_{10}, sea surface temperature, T_s, and salinity, S. Global maps of satellite or *in situ* data for all these variables are available.

SSM/I data sets

SSM/I provides global maps of T_B, U_{10}, V, and L on a daily basis. The SSM/I is a passive microwave sensor flown aboard Defense Meteorological Satellite Program (DMSP) satellites, which detects microwave radiation at four frequencies: 19.35, 22.235, 37.0, and 85.5 GHz. The 19, 37, and 85 GHz channels record v and h polarizations of the radiation, while the 22 GHz channel registers only v polarization, yielding totally seven channels. The 19-GHz channel has the largest footprint (69×43 km^2), i.e., the lowest spatial resolution, and the 85-GHz channel has the smallest footprint (15×13 km^2). The SSM/I orbits the earth about 14 times per day, making ascending (south to north) and descending (north to south) passes.

The raw output voltages of the radiometer are calibrated and converted to antenna temperatures, T_A. The subsequent antenna pattern correction (APC) removes the effects of the antenna sidelobes and converts T_A into brightness temperature, T_B. These T_B values comprise the basic information the SSM/I is collecting from the earth/atmosphere system. Values for U_{10}, V, and L are derived as geophysical products from T_B using Wentz's benchmark Pathfinder algorithm (Wentz, 1997). While T_B values are not corrected for atmospheric effect and the V and L values represent the atmospheric signal, the U_{10} values are for the ocean surface.

The Global Hydrology Resource Center (GHRC) associated with Marshall Space Flight Center (MSFC), NASA, processes daily T_B, U_{10}, V, and L data in full (swath) and reduced (gridded) resolution. Data used in this work are in 0.5°×0.5° (i.e., 54 km × 54 km) gridded maps. Data sets are archived and distributed in Hierarchical Data Format (HDF) files as matrices and images with 720×360 elements and pixels, respectively (http://ghrc.msfc.nasa.gov/ghrc/list.html).

T_B data are scaled and represented in the HDF files as integer numbers. Dividing these numbers by 100 yields a range from 100 to 300 K of valid T_B values for both ocean and land. Figure 3.1a shows data for $T_B(h)$ values measured during ascending passes of SSM/I on 27 March (Julian day 86), 1998.

The geophysical products derived from T_B are presented in the HDF files as real numbers. Valid U_{10} values range from 0 to 40 m s^{-1}, V values are in the range of 0 to 10 g cm^{-2}, and L values are from 0 to 1000 mg cm^{-2}. Global maps of U_{10}, V, and L are shown in Figures 3.1b, c, and d, respectively. For the computations, the units of V [g cm^{-2}] and L [mg cm^{-2}] are converted to [mm] using the relation 1 g $m^{-2}\times10^{-3}$ = 1 mm (Wentz, 1997).

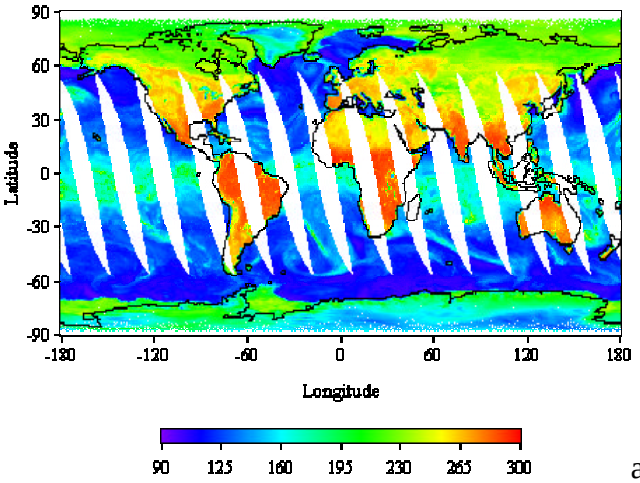

a)

Figure 3.1 a) Brightness temperature, T_B, from SSM/I for 27 March (Julian day 86), 1998; 19 GHz, *h* polarization; ascending passes, map 0.5°×0.5°.

Frequency choice

Since SSM/I operates at four frequencies, it is necessary to choose which f_r, hence $\grave{u}$ and T_B, to use in the calculations of e, e, e_s, and Δe_r. Two criteria help to take this decision.

One criterion is that at the chosen f_r, the changes in ocean surface emissivity should be predominantly due to foam, if present, and not to other factors. According to (3.15-3.16), salinity and temperature of the seawater bring changes in $\mathring{a}$and hence contribute, beside foam, to the variations of the components of ocean surface emissivity and T_B. The influence of salt for frequencies from 1 to 50 GHz on $\mathring{a}$and e is weak for both *h* and *v* polarizations, except at frequencies below 5 GHz (Wilheit, 1978). Over the range of 0-30 °C, the change in T_B per change in T_s,

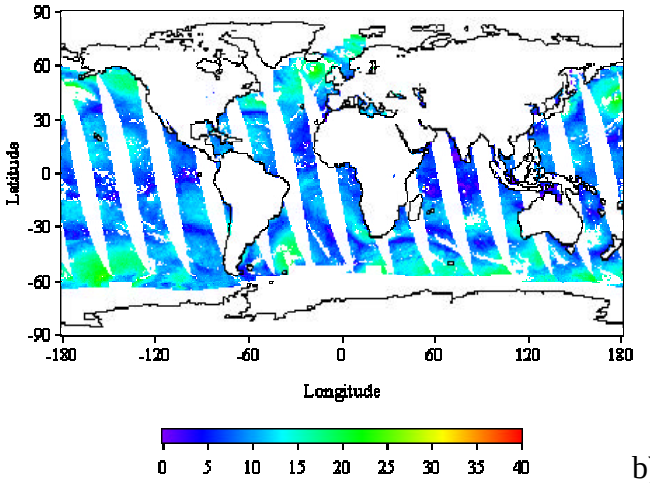

b)

Wind speed, U_{10} (m s^{-1})

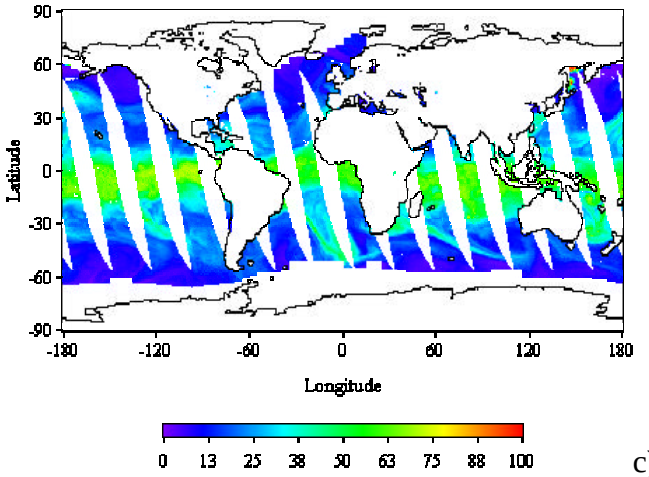

c)

Water vapor, V (mm

Figure 3.1 b) Wind speed, U_{10}, and c) water vapor, V, from SSM/I for 27 March (Julian day 86), 1998; ascending passes, map 0.5°×0.5°.

$\partial T_B / \partial T_s$, as a function of radio frequency follows a nonlinear curve (Wilheit, 1978).

The curve shows that at the incident angle q of SMM/I, T_B values at both h and v polarizations are independent of T_s (i.e., $\partial T_B / \partial T_s = 0$) only for frequencies around 1 and

20 GHz. On the basis of these two statements, the first criterion points to 19 GHz as the most suitable frequency for observing foamy areas.

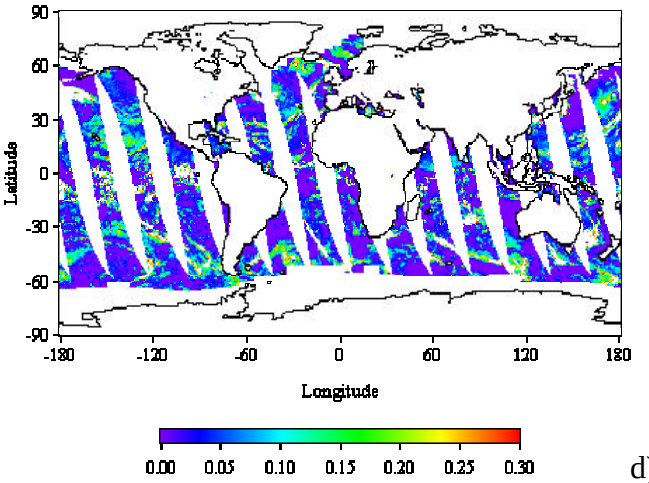

d)
Cloud liquid water, L (mm)

Figure 3.1 d) Cloud liquid water, *L*, from SSM/I for 27 March (Julian day 86), 1998; ascending passes, map 0.5°×0.5°.

The second criterion arises from the need to have as little atmospheric effects as possible at the chosen frequency. The SSM/I frequencies were chosen with specific objectives (Wilheit, 1978; Wilheit and Chang, 1980): the 22-GHz channel is suitable for estimates of atmospheric water vapor; the 85-GHz channel is for effective measure of rain and cloud properties; the 19- and 37-GHz channels are appropriate for evaluation of surface phenomena. Of these two, 19-GHz is a better choice when the first criterion is considered. Indeed, various algorithms use primarily 19*h* and 19*v* GHz, and obtain whatever weighting factors are needed from the 37*h* and 37*v* GHz channels. Thus, the second criterion also singles out the 19 GHz frequency as a suitable choice.

The conclusion from the two criteria, therefore, is: 19.35 GHz frequency would suit the new method purpose best.

Another choice to make is which polarization of T_B data, *h* or *v*, to use. To make this choice it is necessary to identify at which polarization the changes in ocean surface emissivity and T_B due to the appearance of foam are more noticeable. Radiometric experiments and models investigating the effect of wind speed on ocean surface emissivity and T_B have shown that the *h* polarization of T_B has higher sensitivity to changes in surface wind speed (Hollinger, 1971; Webster and al., 1976; Wilheit, 1978; Pandey and Kakar, 1982; Wang et al., 1995). Although the absolute values of the vertically polarized T_B are greater than the horizontally polarized T_B values, the $T_B(U_{10})$ plots reported for *h* polarization are steeper than those for *v*. Indeed, a 1-m s^{-1} change of wind speed invokes a change of about 0.5 K in vertically polarized T_B while horizontally polarized T_B changes with about 1.2 K. The reasons for such difference in the sensitivity of both polarizations are that at *h* polarization i) the effects of both roughness and foam increase with increasing wind speed, and ii) the emissivity of the undisturbed surface decreases thereby increasing the emissivity contrast between the foam and open water. At *v* polarization, the effects of roughness and foam are relatively weak yielding low sensitivity at this polarization (Wilheit, 1978). The choice, therefore, is to use data for horizontally polarized T_B.

AVHRR T_s data

The AVHRR provides global maps of sea surface temperature, T_s, on a daily basis. The AVHRR aboard currently flying NOAA-14 polar orbiting satellite is a visible/infrared multispectral scanner, which registers the earth/atmosphere radiation in five channels. After calibration, a nonlinear algorithm derives T_s data from the difference

of the brightness temperatures in channels 4 (10.3-11.3 μm) and 5 (11.5-12.5 μm), an initial estimate of the SST field, and coefficients calculated for different water vapor regimes. Several versions of the processing algorithm exist, all aiming to improve the evaluation of these coefficients. A series of statistical tests establishes the quality of each SST value.

The Physical Oceanography Distributed Active Archive Center (PO.DAAC) at the Jet Propulsion Laboratory (JPL), NASA, distributes T_s data in several spatial and temporal resolutions for both ascending and descending passes. Daily and monthly averaged SST values are offered in two main modes, best SST and all-pixel SST at spatial resolutions of 9 km (4096×2048 pixels), 18 km (2048×1024) and 54 km (720×360). For consistency with the resolution of the SSM/I data sets, T_s data at 54 km×54 km resolution are used in this study. While the all-pixel SST product contains all estimated SST values regardless of their quality, best SST product retains only pixels with the highest quality, discarding areas with clouds and areas from the far and distorted portion of the swath. Data sets with the best SST values are used in the new method calculations.

Data are offered in various formats including HDF. The HDF files contain byte arrays of dimensions depending on the spatial resolution, 720×360 for this study (http://podaac.jpl.nasa.gov/sst/sst_data.html). The elements in the arrays, named digital numbers (DN), must be scaled with a conversion equation:

$$\mathrm{SST} = 0.15\ \mathrm{DN} - 3.0 \tag{3.21}$$

to obtain appropriate SST in °C. The DNs have values from 0 to a possible maximum of 255, where 0s fill cells with missing data, and 1-255 are DNs giving meaningful SST values.

The DN numbers in AVHRR data sets are first converted into meaningful T_s values using (3.21). The range of possible SST is from –2.85 to 35.25 °C. Both these limits seem unrealistic, but, in concord with AVHRR intended design, the range includes climatologically realistic as well as anomalously extreme events. While inspection of the value distributions of daily T_s does not encounter cells with temperature higher than 33 °C, T_s values as low as –2.85 to –1.95 °C are always present. At a salinity of 35 psu the temperature of the freezing point of the water is –1.91 °C. According to WOA98, regions with cold waters have a maximum S of 34.2 psu, and T_s less than –1.91 °C cannot be expected. Òhe SST algorithm does not have an explicit flag for sea ice, thus the most probable reason for retrieving such low temperatures as valid T_s values is the presence of seawater mixed with ice (slush). Though meaningful, cells with DNs from 1 to 7, giving extremely low SST values, are discarded in this study, because the emission of ice is as high as that of whitecaps and the new method cannot distinguish their signals. With that, the range of T_s is –1.8 to about 33 °C. For day 86, the discard of $T_s < -1.8$ removes about 2% of all available T_s values.

T_s is in °C for the computation of e_s and e_f, and is converted to K for e and Δe_r. Figure 3.2a shows a map of valid T_s in °C. Note in the figure the lack of complete coverage *within* satellite passes—a consequence of using the PO.DAAC product of the best T_s values. Because all other data sets exhibit more complete coverage (compare with Figure 3.1), the daily T_s maps determine the cell number and locations for which all necessary data exist and match. Thus, from each T_s map, a mask containing pixels available for the computations is created for each day.

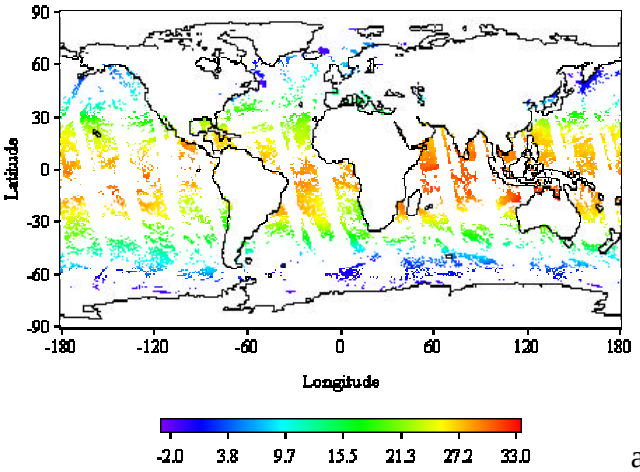

a)

Sea surface temperature, T_s (°C)

Figure 3.2 a) Sea surface temperature, T_s, for 27 March (Julian day 86), 1998, ascending passes; map is 0.5°×0.5°.

WOA98 S data

The WOA98 provides global maps of seawater salinity, *S*, at 33 standard levels covering depths from 0 to 5500 m (Levitus et al., 1998). The WOA98 is based on the extensive World Ocean Database 1998 (WOD98) of the National Oceanographic Data Center (NODC), Ocean Climate Laboratory (OCL). WOD98 contains more than 4 million data entries compiled from many different sources, programs, and even individual scientists, from countries all over the world. The salinity data alone have 1,343,580 entries in WOD98, measured since 1874 with various instruments including historical oceanographic records, bottle seawater samples (ocean station data), and conductivity-temperature-depth (CTD) instruments.

The global salinity maps presented in the WOA98 for each depth level result from several processing steps. First, the discrete salinity data available from vertical profiles taken at various locations of the world ocean were subject to numerous quality

control checks. Next, the quality *S* data were averaged on a 1°×1° global grid to form input to an objective analysis program. The objective analysis program produces a global salinity field for each standard level by interpolation. The Atlas contains several final products, climatological mean *S* fields among them, averaged monthly, seasonally, and annually.

Data are offered as text files, representing *S* values as real numbers. A file for a given product contains several "stacked" 10×6480 arrays, one for each depth level (http://www.nodc.noaa.gov/OC5/data_woa.html). The new method uses 1°×1° maps of monthly climatological means of *S* at the surface, i.e., the first 10×6480 array in a file for a given month.

The salinity sets require several rearrangements. First, from a file for a given month the first 10×6480 array in the stack, containing *S* values for the surface layer, is extracted. Next, this array is rearranged into 360×180 array to represent the true latitude-longitude configuration in 1°×1° map. Then, this array is re-sampled via bilinear interpolation to obtain an array of 720×360 elements, i.e., a 0.5°×0.5° map, consistent with the data sets from SSM/I and AVHRR. The re-sampling causes the appearance of spurious *S* values along the continental edges where the interpolation between land values (99.999) and valid *S* values results in higher salinity. To recognize the cells with such spurious values and remove them, the re-sampling procedure *a priori* recodes the land values to −10,000. Finally, the map is shifted with 360 columns to unify the global view of the salinity maps with that of the other data sets. A contour plot of the land is constructed from the salinity maps and later overlapped to all other data sets. Figure 3.2b shows the salinity map for March 1998 resulting from all these procedures.

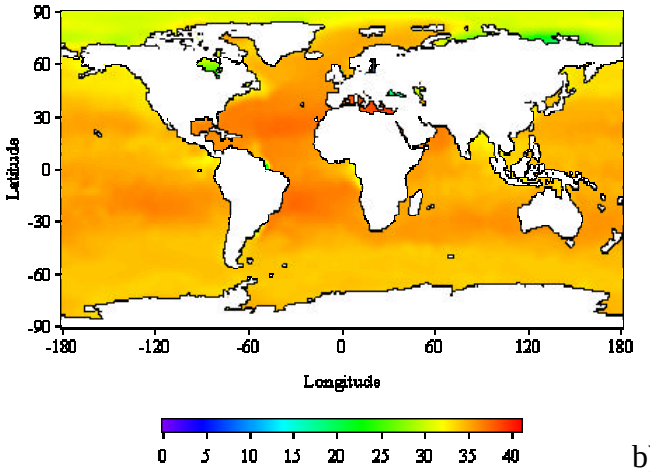

b)

Figure 3.2 b) Seawater salinity, *S*, for March 1998. Map is 0.5°×0.5°.

Data preparation

Data sets of T_B, V, L, U_{10}, and T_s for all 365 days and S for all 12 months of 1998 were ordered from the respective data centers, transferred through FTP, and archived for later use. Next, all initial data manipulations, described in the previous sections, are applied to obtain consistency in the spatial resolution, validity of the values, unification of the units, and availability of matching data. Finally, wind, clear sky, and rain masks are prepared for each day and applied to all data sets. The construction of the masks is described below.

The wind mask is extracted from a daily U_{10} map. The wind mask favors cells with wind speeds ≥ 3 m s^{-1}, the wind speed for whitecap inception, and discards (puts 0s) in cells with lower wind. Very high winds, $U_{10} > 35$ m s^{-1}, though valid, are also excluded since the SSM/I is not designed for high winds and its performance deteriorates under gale conditions. Figure 3.3a demonstrates the effect of the wind mask

when applied to the $T_B(h)$ map for day 86 shown in Figure 3.1a. The wind mask removes about 2% of the pixels representing the ocean.

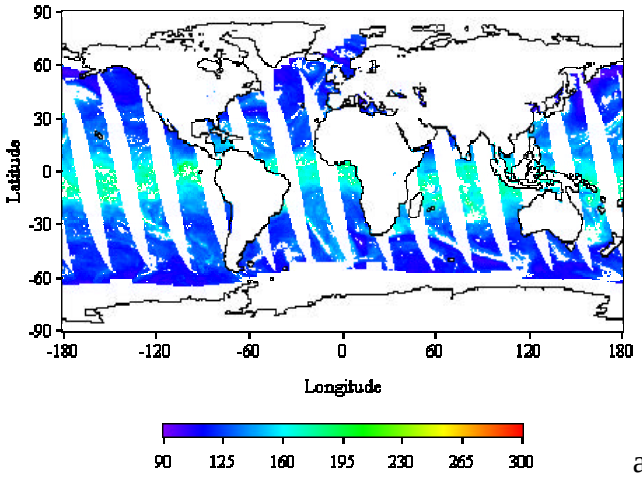

a)

Figure 3.3 a) Effect of wind mask on $T_B(h)$ for Julian day 86, 1998 (compare with 3.1a).

The clear sky mask, prepared from daily L maps, discards the cells with high content of cloud liquid water. According to Wentz et al. (1980), clear sky cells are those for which $L \leq 5$ mg cm^{-2} = 0.05 mm. Figure 3.3b shows the effect of the clear sky mask on the $T_B(h)$ map for day 86. About 40% of the "ocean" pixels contaminated with clouds are removed from the map uniformly. For the remaining 60% of "ocean" pixels, the assumption $L = 0$ holds, which changes the attenuation coefficient due to clouds in (3.10) to $a_L = 0$. This yields a modified attenuation coefficient, k, in (3.7b):

$$k = a_O + a_V .$$

Since the atmospheric transmittance obtained with (3.7-3.10) is for a nonraining atmosphere, a rain mask is necessary. A cell is considered rain-free when

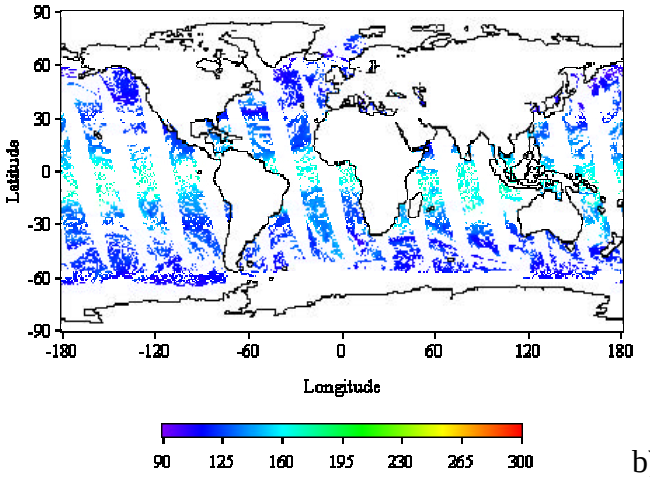

Figure 3.3 b) Effect of clear sky mask on $T_B(h)$ for Julian day 86, 1998 (compare with 3.1a).

two requirements, formed from *h* and *v* polarizations of T_B at 19 and 37 GHz, are fulfilled simultaneously (Goodberlet et al., 1989):

$$T_B(37v) - T_B(37h) > T_0 \quad \textit{and} \quad T_B(19h) > T_1 \tag{3.22}$$

where T_0 and T_1 have different values depending on the latitude (Table A.3). Once again, the effect of the rain mask is demonstrated on the map of $T_B(h)$ for day 86 (Figure 3.3c). The rain mask removes about 14% from the useful "ocean" pixels. Comparison of Figure 3.3c with Figure 3.1a reveals that apparently most of the removed cells are associated with high T_s, which could introduce bias in the distribution of T_s values toward lower temperatures. Figure 3.3d displays the distributions of T_s for day 86 without (black bars) and with (white bars) the mask applied, and the percentage of removed cells for each temperature bin (solid line with

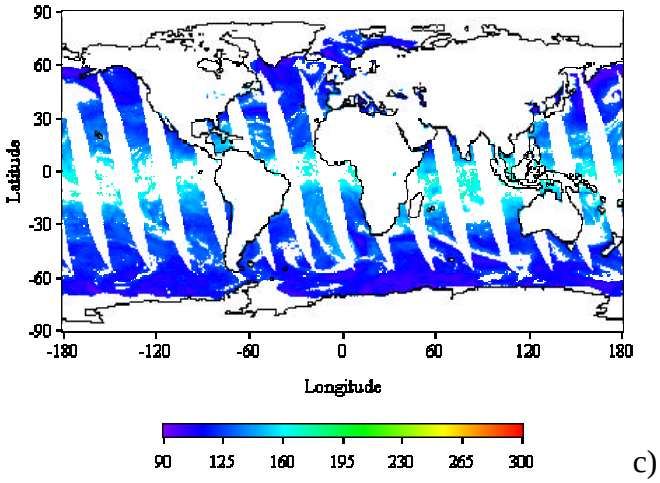

c)

Brightness temperature, T_B (K)

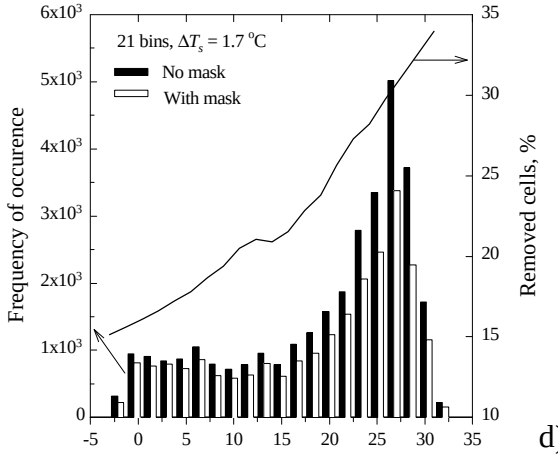

d)

Sea surface temperature, T_s (°C)

Figure 3.3 **c) Effect of rain mask on $T_B(h)$ for Julian day 86, 1998 (compare with 3.1a); d) Distributions of T_s values without (black bars) and with (white bars) rain mask applied, and percentage of cells removed by the mask at various T_s values (solid line and axis at right).**

axis at right). Indeed, the rain mask removes more cells with T_s in the range of 25-33 °C (e.g., about 34%) than with lower T_s values (less than 25%). The shape of the masked

distribution, however, does not change significantly compared to the initial distribution; there is not noticeable skewness toward lower T_s values. In addition, the averages of the initial (20.02 °C) and masked (19.22 °C) T_s values differ by 4%. Thus, despite the apparently preferential removal of high T_s, the effect of the rain mask is still tolerable and brings more use than harm.

These three masks (for wind, clear sky, and rain), together with the mask giving the cells with available T_s, combine to form one composite mask. This composite mask is applied to S, T_s, T_B, U_{10}, and V, and with that, all necessary data sets are ready for the computation of the emissivities and W. Figure 3.4a shows the cells left after applying the composite mask on the T_B map for day 86, and the distribution of the T_B values available for further calculations is in Figure 3.4b. The composite mask removes about 83% (!) of the initial ocean pixels, leaving about 15,800 cells available for W estimation in that particular day. For all days of 1998, the numbers of removed and useful cells are of the same order. Thus, calculations of W for each day of 1998 would provide an enormous amount of data adequate to prepare an extensive database of whitecap coverage and concomitant meteorological parameters. Maps and distributions for U_{10}, S, T_s, and V after applying the composite mask are presented in Figures 3.5-3.8.

3.2.3 Error analysis

The new method uses many measured and calculated quantities to estimate global whitecap coverage, W. Uncertainties in data measurements are carried over the calculated variables, and ultimately to the final result. Thus, to determine the uncertainty with which the new method retrieves W, an analysis of the error propagation and the contributions of the various quantities to the error of W has to be

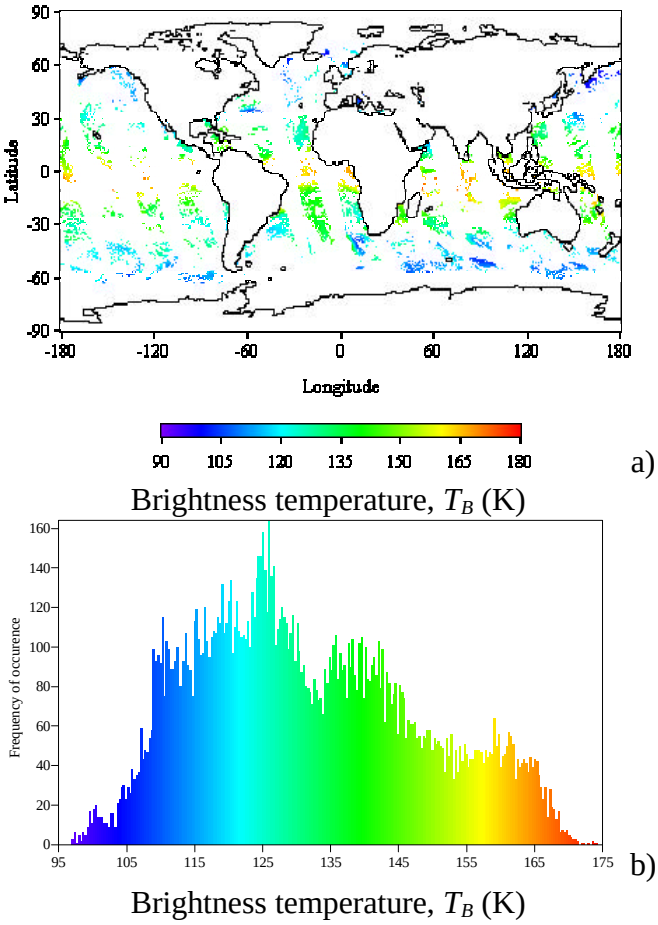

Figure 3.4 **a) Effect of the composite mask on $T_B(19h)$ for day 86 (27 March), 1998, map 0.5°×0.5°; b) Distribution of $T_B(19h)$ values left after applying all masks.**

made. This analysis will help to establish conditions under which *W* could be obtained with an acceptable error, and to identify causes restricting accurate retrieval of *W*.

Error analysis principles

Two approaches for analyzing error propagation have been described in the literature. One of these approaches gives error expressions in terms of variance

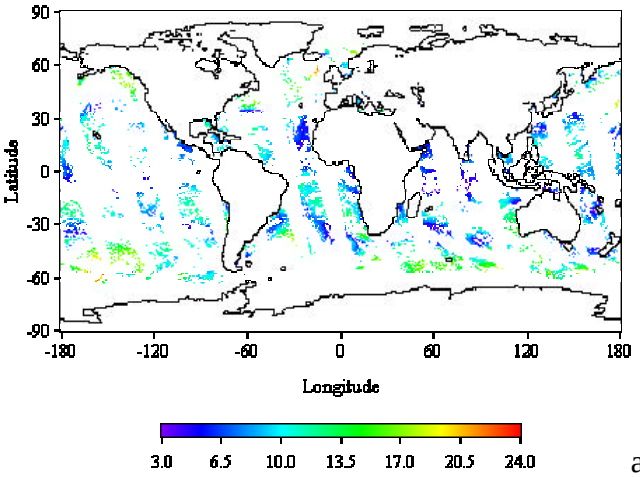

a)

Wind speed, U_{10} (m s^{-1})

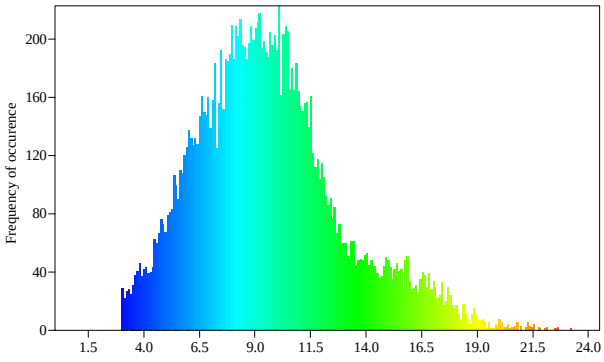

b)

Wind speed, U_{10} (m s^{-1})

Figure 3.5 **a) Effect of the composite mask on U_{10} for day 86 (27 March), 1998, map 0.5°×0.5°; b) Distribution of U_{10} values left after applying all masks.**

(Bevington, 1969; Clifford, 1973; Bragg, 1974), while the other approach gives the error expressions in terms of relative error (Clifford, 1973; Bragg, 1974; Andreas, 1991). The variance of a quantity x is defined as:

$$s_x^2 = \frac{1}{N}\sum_{i=1}^{N}(x_i - \bar{x})^2$$

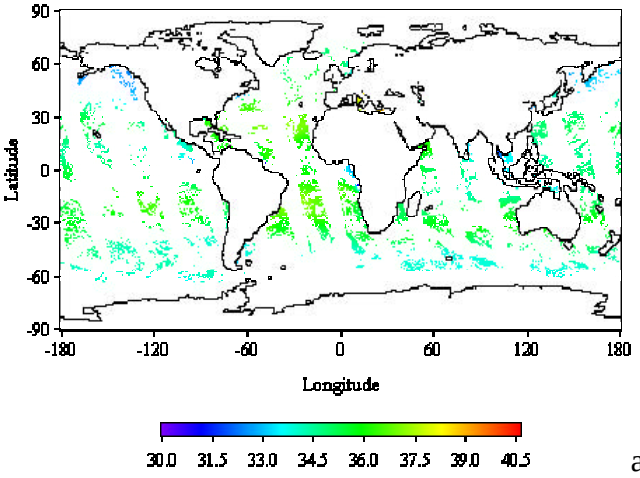

a)

Salinity, *S* (psu)

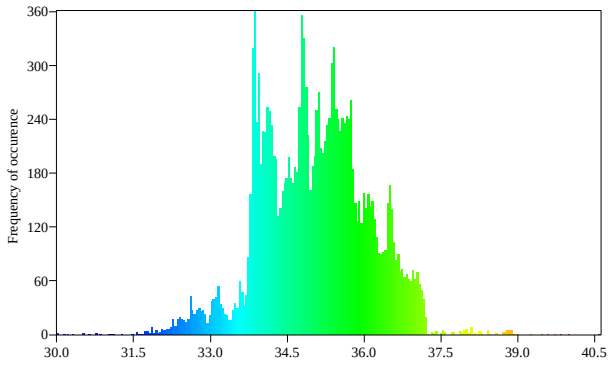

b)

Salinity, *S* (psu)

Figure 3.6 **a) Effect of the composite mask on *S* for day 86 (27 March), 1998, map 0.5°×0.5°; b) Distribution of *S* values left after applying all masks.**

called also the root mean square (rms) error. The relative error of a quantity x is defined as $r.e._x = s_x / \overline{x}$. While the standard deviation usually bears the units of the variable it

characterizes, e.g., V [mm] ± s_V [mm], the relative error is usually given as a percentage, e.g., V [mm] ± $r.e._V$%.

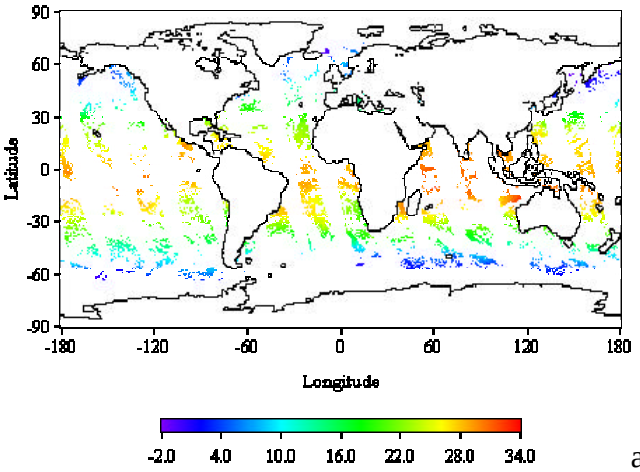

a)

Sea surface temperature, T_s (°C)

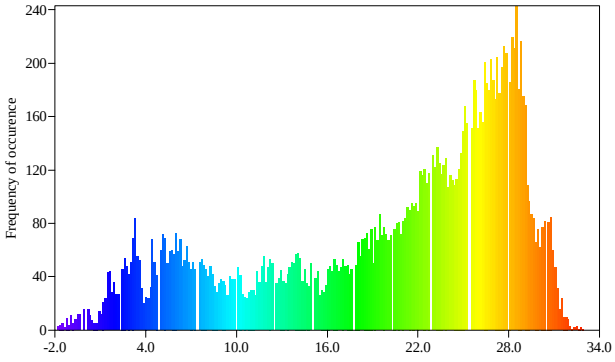

b)

Sea surface temperature, T_s (°C)

Figure 3.7 a) Effect of the composite mask on T_s for day 86 (27 March), 1998, map 0.5°×0.5°; b) Distribution of T_s values left after applying all masks.

Both standard deviation and relative error are equally common in expressing the uncertainty of a variable, and given one of them, the other can be always obtained.

This interchangeability is one of the arguments supporting the decision to use the variance approach in this study. In addition, the uncertainties of most of the variables involved in *W* calculations are given in terms of variance or standard deviation.

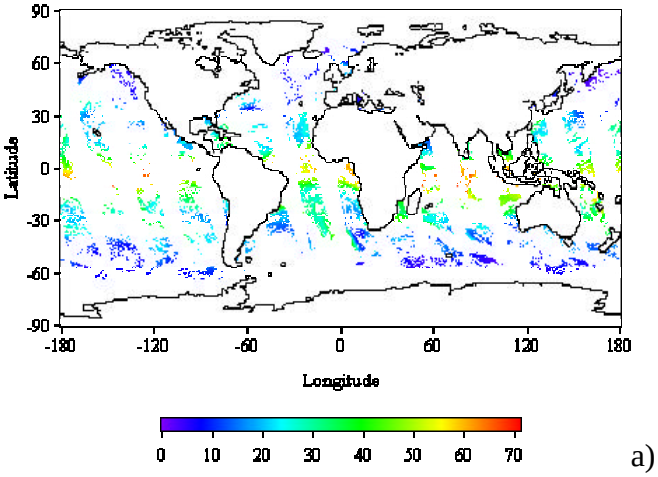

a)

Water vapor, *V* (mm)

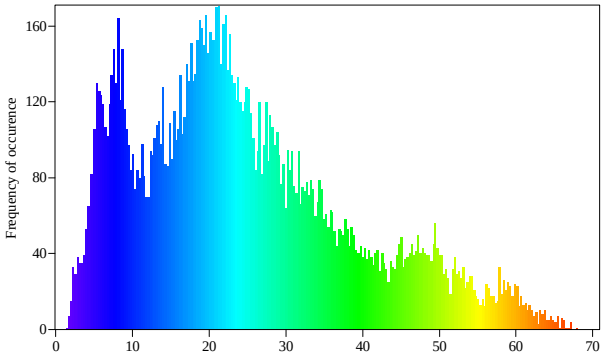

b)

Water vapor, *V* (mm)

Figure 3.8 **a) Effect of the composite mask on *V* for day 86 (27 March), 1998. Map 0.5°×0.5°; b) Distribution of *V* values left after applying all masks.**

Let the quantity necessary to be determined be *x*, which is a function of at least two other measured variables *u* and *v* (Bevington, 1969):

$$x = f(u, v, \ldots)$$

The variance s_x^2 for *x* in terms of the variances s_u^2, s_v^2, … for the measured variables *u*, *v*, … is expressed as:

$$s_x^2 \cong s_u^2 \left(\frac{\partial x}{\partial u}\right)^2 + s_v^2 \left(\frac{\partial x}{\partial v}\right)^2 + 2 s_{uv}^2 \left(\frac{\partial x}{\partial u}\right)\left(\frac{\partial x}{\partial v}\right) + \ldots, \qquad (3.23)$$

where s_{uv}^2 is the covariance between the variables *u* and *v* defined as (Bevington, 1969; Greenberg, 1988, p. 31):

$$\left| s_{uv}^2 \right| = \frac{1}{N} \sum_{i=1}^{N} \left[(u_i - \bar{u})(v_i - \bar{v}) \right] \leq s_u s_v .$$

If it is assumed that the fluctuations in measuring *u* and *v* are uncorrelated, the covariance term could be dropped. The partial derivatives forming the coefficients $(\partial x/\partial u)^2$, $(\partial x/\partial v)^2$, $(\partial x/\partial u)(\partial x/\partial v)$, … are called sensitivity coefficients and are measures of the contribution of the variances to which they are attached (Andreas, 1991). They are evaluated with all other variables fixed at their mean values (Bevington, 1969). When additional variables besides *u* and *v* determine *x*, their contributions to the variance of *x* have terms similar to those in (3.23).

Derived error expressions

The variance approach is applied to all expressions (3.4-3.20) to evaluate the propagation of error. The analysis of each investigated quantity starts with two considerations (Appendix C): 1) on which variables this quantity depends, and 2) which covariant terms are likely to play a role. Next, the analysis proceeds with deriving a general error expression for the variance of the investigated quantity by applying (3.23)

to all formulas used for *W* calculation. Finally, each specific variable, on which the considered quantity depends, is substituted in the general error expression with all other variables fixed (i.e., constant), yielding the analytical forms of the sensitivity coefficients for each variable.

The error analysis derives variance of calculated *W*, s_W^2, as a function of the variances of the four emissivities and two covariant terms:

$$s_W^2 \le W_e s_e^2 + W_s s_{e_s}^2 + W_f s_{e_f}^2 + W_r s_{e_r}^2 + 2W_{er} s_e s_{e_r} + 2W_{sf} s_{e_s} s_{e_f} \qquad (3.24)$$

where the sensitivity coefficients are calculated using the computed emissivities:

$$W_e = \frac{1}{(e_f - e_s - \Delta e_r)^2} \qquad W_f = \frac{(e - e_s - \Delta e_r)^2}{(e_f - e_s - \Delta e_r)^4}$$

$$W_s = \frac{(e - e_f)^2}{(e_f - e_s - \Delta e_r)^4} \qquad W_{er} = \frac{e - e_f}{(e_f - e_s - \Delta e_r)^3} \qquad (3.25)$$

$$W_r = \frac{(e - e_f)^2}{(e_f - e_s - \Delta e_r)^4} \equiv W_s \qquad W_{sf} = -\frac{(e - e_f)(e - e_s - \Delta e_r)}{(e_f - e_s - \Delta e_r)^4}$$

The same procedures are applied to obtain the variance of each emissivity (s_e^2, $s_{e_s}^2$, $s_{e_f}^2$, and $s_{e_r}^2$) as a function of the basic variables whose measurement errors influence them.

Overall, there are 9 basic variables, namely T_B, V, U_{10}, T_s, S, $e_¥$, s, q, and Q, whose errors propagate to the errors of the emissivities. Appendix C (section C.1) briefly summarizes the reasons causing the errors in measuring or retrieving these variables. In addition, section C.1 comments how improvement in satellite technology and measurements would in turn improve these errors in future. Tracking the functional dependencies entering expressions (3.5-3.10) identifies the basic variables affecting *e*.

Appendix C clarifies this procedure. As a result, seawater emissivity emerges as a function of four basic variables, $e = f(T_B, T_s, V, q)$. Tracking (3.11-3.16), gives $e_s = f(T_s, S, q, s, e_{¥})$. For foam emissivity, the void fraction adds to this list, $e_f = f(T_s, S, q, s, e_{¥}, Q)$. Rough-sea emissivity depends on three variables, $\Delta e_r = f(T_s, U_{10}, q)$. Finally, taking into account possible co-variations (Appendix C), the variances of the four emissivities in (3.2) are derived as:

$$
\begin{aligned}
s_e^2 &\le E_{eB} s_{T_B}^2 + E_{eT} s_{T_s}^2 + E_{eV} s_V^2 + E_{eq} s_q^2 + \\
&\quad + 2E_{BV} s_{T_B} s_V + 2E_{Bq} s_{T_B} s_q + 2E_{Vq} s_V s_q \\
s_{e_s}^2 &= E_{sT} s_{T_s}^2 + E_{sS} s_S^2 + E_{sq} s_q^2 + E_{ss} s_s^2 + E_{s\infty} s_{e_\infty}^2 \\
s_{e_f}^2 &= E_{fT} s_{T_s}^2 + E_{fs} s_s^2 + E_{fq} s_q^2 + E_{fs} s_s^2 + E_{f\infty} s_{e_\infty}^2 + E_{fQ} s_Q^2 \\
s_{e_r}^2 &\le E_{rT} s_{T_s}^2 + E_{rU} s_U^2 + E_{rq} s_q^2 + 2E_{Uq} s_U s_q
\end{aligned}
\qquad (3.26)
$$

In (3.26), E_{ej}, E_{sj}, E_{fj}, and E_{rj} are the sensitivity coefficients for e, e_s, e_f, and Δe_r, respectively. The index j has different notations, which show the basic variables contributing to the emissivity errors. Each of the sensitivity coefficients, E_{ij}, is determined by a set of expressions containing numerous terms. These terms, in turn, appear as sensitivity coefficients in the variances of the variables involved in the calculations of the emissivities.

Products of the standard deviations of the variables involved in the covariant terms give estimates of the covariances in (3.24) and (3.26). According to the Schwarz inequality, $\left|\sigma_{uv}^2\right| \le \sigma_u \sigma_v$, thus such an estimation of the covariances leads to the inequalities in (3.24) and (3.26). These inequalities reflect not so much a change in the sign of the variances at the left sides of (3.24) and (3.26), but possible changes in the

magnitudes of the right sides. Since all standard deviations used are positive, the magnitudes the right sides depend on the signs of the sensitivity coefficients in the covariant terms. When they are negative, e.g., W_{er} in (3.24) and E_{BV} and E_{Bq} in (3.26), the right sides of the respective equations in (3.24) and (3.26) decrease in magnitude, and the respective variances at left are smaller. When the sensitivity coefficients in the covariant terms are positive, e.g., W_{sf} in (3.24) and E_{Vq} and E_{Uq} in (3.26), the right sides of the respective equations in (3.24) and (3.26) increase in magnitude, rendering higher variances at left. Equations (3.24) and (3.26) contain the net result of these opposing tendencies and show that the variances of W, e, e_s, e_f, and Δe_r could be at most the values estimated with the right sides or lower.

The variances and standard deviations of the basic variables are either known from their measurement and calculation or are chosen. Table A.4 lists values of all standard deviations involved in (3.24) and (3.26).

3.3 Results

Having all necessary analytical and error expressions, initial values, and prepared data at hand, the calculation of the emissivities, and then of W, begin. The calculations proceed in the environment of the software *Transform* with its specialized Fortran-like language. *Transform* software is one of several units in the *Noésys* package, which is the first commercial product for working with HDF files.

The algorithm for retrieving W is implemented with a package of programs called sequentially by a main program. All programs are grouped in 5 units, each performing a major procedure. The main unit runs a loop for all days in a month and calculates W. It first calls a unit of programs constructing all masks; next, it turns to another unit to calculate all different emissivities; then it addresses a unit evaluating the

errors. Intermediate arrays, resulting from these units, are used to calculate daily W on a global map. Finally, the main program calls a unit, which re-arranges the retrieved W and some accompanying environmental variables in large matrices ready for further analysis.

The distributions of the basic data sets (panels b in Figures 3.4 to 3.8) help to identify the most frequently occurring values for T_B, U_{10}, S, T_s, and V. These values are used as parameters to perform an analytical investigation of expected values for all four emissivities in (3.2), W, and their errors (3.24-3.26).

The actual performance of the new method is tested with data for one day. All results given below in sections "Observations" are for the ascending passes on 27 March (Julian day 86), 1998.

3.3.1 Emissivities

Analytical investigation

The values of e, e_s, Δe_r, and e_f could be plotted differently considering the variables on which they depend, Figure 3.9. Figure 3.9a displays all emissivities as functions of T_s (a variable common for the calculations of all four of them) under clear skies, L = 0 mm. All emissivities decrease over the range of possible T_s. Plotting the emissivities over a scale from 0 to1 in the figure does not emphasize the changes with water temperature. Rather, it reveals well the relative difference between their values. At fixed S = 35 and for T_s from –2 to 33 °C, e_s (red line) changes from 0.288 to 0.258, but remains relatively low conforming to the contention that in the microwave range a smooth flat ocean is a cold body with low emissivity. At the same S and the chosen Q = 2%, e_f decreases from 0.944 to 0.915 (blue line) keeping its high value (close to the

emission of a black body, as expected from the theory) over the entire range of T_s. Over the range of T_s at U_{10} = 9 m s^{-1}, surface roughness adds to the specular emissivity little but a measurable correction of about Δe_r = 0.031 (green line). At V = 20 mm and T_B = 125 K, seawater emissivity, e (black line), decreases from 0.345 to 0.291. Over the entire T_s range, e is larger than $e_s + \Delta e_r$ (pink line). This is expected because e represents both foam-free and foam-covered surface, while $e_s + \Delta e_r$ is the emissivity of a rough but foam-free sea.

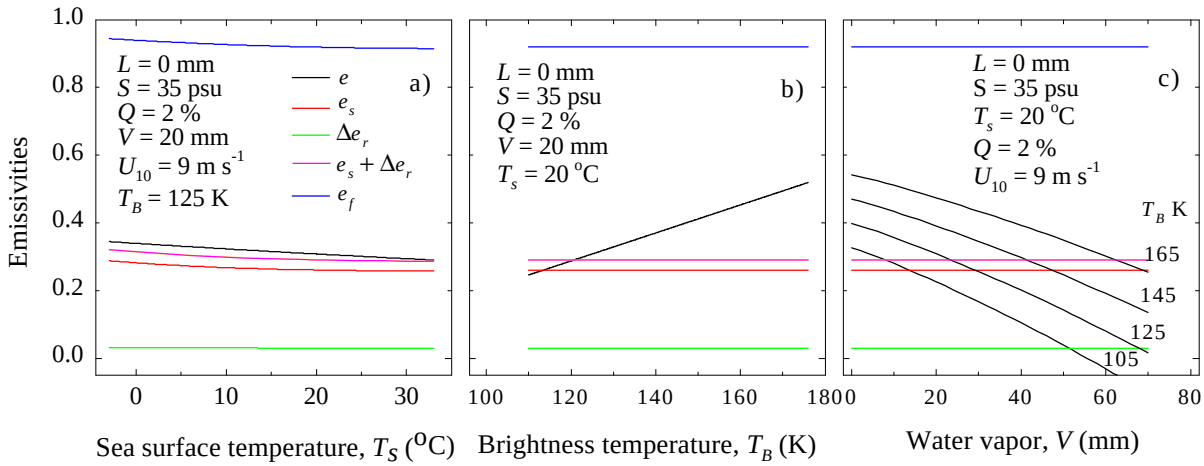

Figure 3.9 All emissivities in (3.2) under clear sky (L = 0 mm) at most frequently occurring S, T_B, V, and U_{10} as functions of: a) T_s; b) T_B; c) V at various T_B.

Figure 3.9b depicts the emissivities as functions of T_B. Actually, only e varies with T_B (e_s, Δe_r, and e_f do not depend on T_B), but this view reveals an interesting feature: a crossing point between e and e_s at about T_B = 112 K. This crossing point shows that combinations of T_B, U_{10}, S, T_s, and V could be expected for which e becomes

less than e_s. It is physically unrealistic to observe seawater emissivity, e, lower than the specular emissivity, e_s. The specular emissivity, e_s, is the lowest possible value for ocean emission (note that Δe_r is a *correction* term, it adds to e_s to give the emissivity of rough sea). Thus, only the values of e for $T_B > 112$ K are valid in Figure 3.9b.

A plausible explanation of encountering e values that are too low is the effect of V. In a humid atmosphere, the atmospheric signal becomes so strong that it masks the ocean surface signal. Analytically, the atmospheric terms in (3.4), those including T_{BU}, T_{BD}, and T_{CB}, are estimated using V. When they become larger than the surface term, described with T_B, they overdo the atmospheric correction, thus giving low e. The effect of the intervening atmosphere is shown in Figure 3.9c, where all emissivities are plotted as functions of V at various T_B. At the given combination of parameters and $T_B = 105$ K, e is lower than e_s for $V > 8$ mm. As T_B increases, the limiting point of retrieving valid e is pushed toward higher V. Physically this means that *low* ocean emission can be detected correctly only in a dry atmosphere; *high* ocean emission can be registered even through a wet atmosphere.

An overall conclusion of this analytical investigation is that humid atmospheric conditions will restrict reliable detection of low ocean emissivity.

Observations

Do these analytical considerations of the validity of e occur in a real situation? Emissivities are calculated with the new algorithm with actual data for 27 March 1998. Figure 3.10 compares values of e (black circles) and $e_s + \Delta e_r$ (yellow circles) along the North-South line at 83° East. Panel a confirms that e becomes too low (green circles) for high V, 63 to 66 mm. These same low e values are associated with low, up to 5.2 m s^{-1}, winds (panel b), and high T_B values, from 165 to 168 °K, panel c.

High T_B values in this and similar cases are logical because only high T_B can accommodate both strong signal from the atmosphere *and* some signal from the ocean surface due to whitecapping. Finally, panel d in Figure 3.10 demonstrates that locations with high V and T_B, are also characterized by low winds.

The results in Figure 3.10 confirm the conclusion of the analytical considerations in Figure 3.9 and help to identify one reason for unreliable detection of e and W: coupling of low wind speed with high humidity—conditions usually found at low latitudes. Scrutinizing more cases of $e < e_s + \Delta e_r$, however, reveals that these conditions are not the only ones restricting the retrieval of valid e and W. Low e values are encountered also in cases characterized with moderate winds (5–10 m s^{-1}) and not so high humidity (15–35 mm) at mid latitudes and in coastal zones. Such results broaden the range of restricting conditions. It proved difficult, however, to identify specific combinations of variables (wind, humidity, water temperature, salinity) responsible for invalid e. Since these restricting combinations of variables vary with location, numerous restricting conditions can be encountered and for now it is not possible to predict where and what restrictions in estimating W may occur.

Figure 3.11 displays global maps of the emissivities for 27 March 1998. To reveal better specific patterns, the emissivity scales are stretched over the ranges of valid values for each emissivity. Seawater emissivity, e, is calculated with (3.4-3.10). Figure 3.11a shows that e ranges from 0.25 to 0.45. Comparison of the patterns in Figures 3.11a and 3.1b shows that e, as expected, exhibits a strong correlation with the U_{10} values. This is a good first check of the validity of e—after all, the retrieval of U_{10} from SSM/I relies on changes of T_B due to changes in e. Specular emissivity, e_s, is

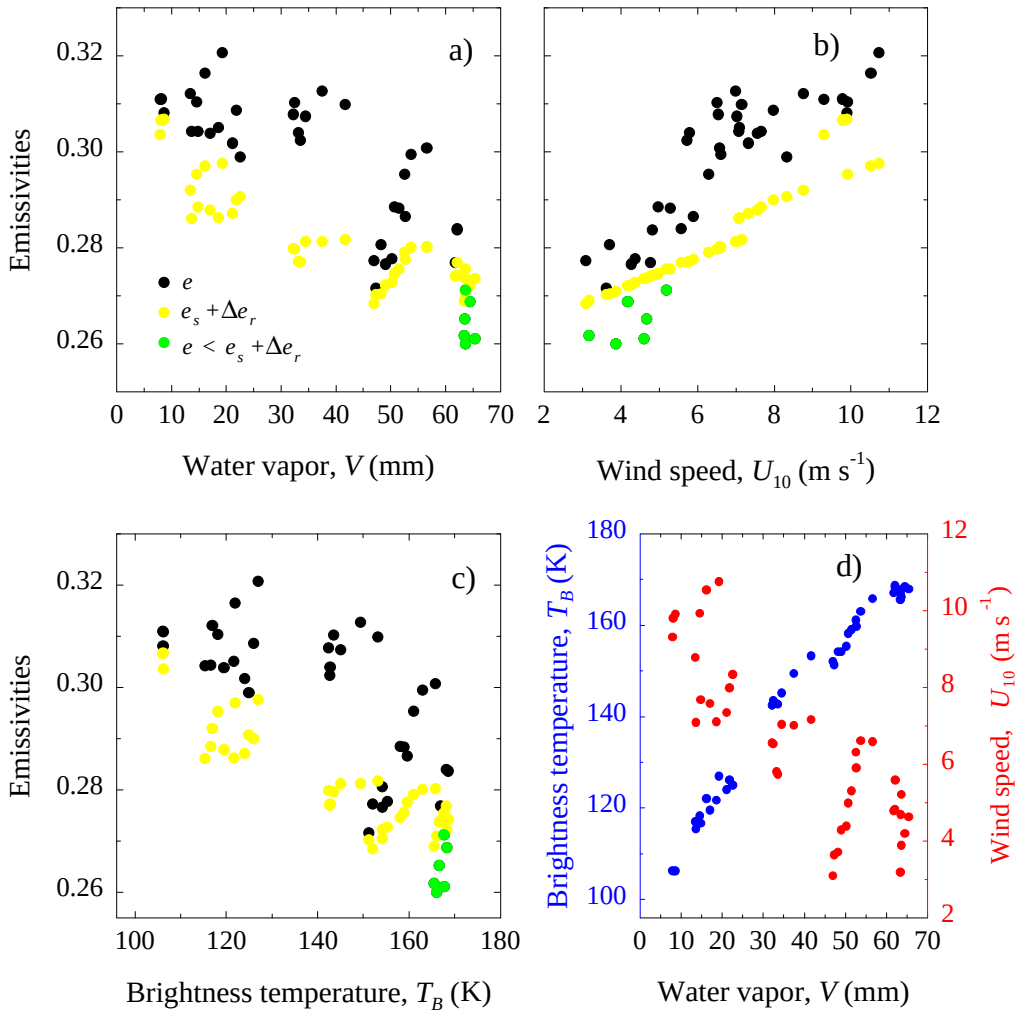

Figure 3.10 Demonstration of the effect of intervening atmosphere with real emissivity values. Comparison of e and $e_s + \Delta e_r$ over the observed range of: a) water vapor, V; b) wind speed, U_{10}; c) brightness temperature, T_B; d) observed T_B and U_{10} values over the range of observed V.

calculated with (3.11-3.16). Figure 3.11b shows that e_s varies from 0.255 to 0.285. Though e_s varies over a narrow range, the comparison of Figures 3.11b and 3.2a shows that it mimics the pattern of T_s inversely. Such behavior is expected since T_s influences e_s

via the dielectric constant (recall 3.14-3.16). The effect of S (compare with Figure 3.2b) is less noticeable, yet is surely present. Emissivity due to roughness, Δe_r, is calculated with (3.17). Figure 3.11c depicts that Δe_r ranges from 0.0095 to0.0832. The influence of both U_{10} and T_s, suggested by (3.17), is well noted when

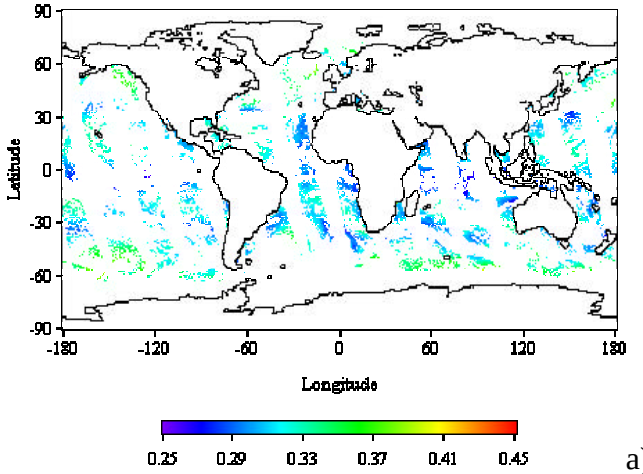

a)

Seawater emissivity, e

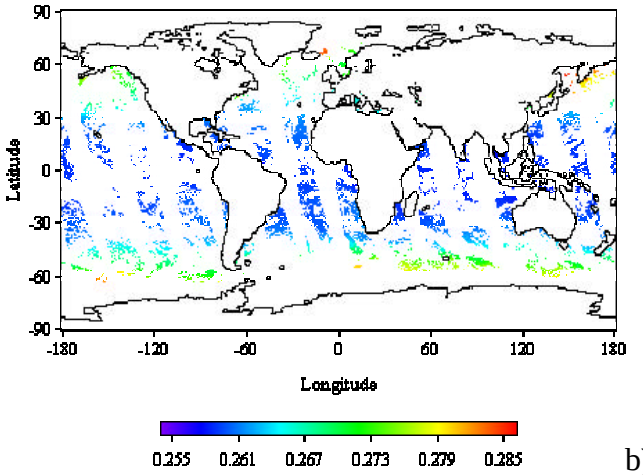

b)

Specular emissivity, e_s

Figure 3.11 Seawater emissivity, e (a), and specular emissivity, e_s (b), for 27 March (Julian day 86), 1998; maps 0.5 °×0.5 °.

patterns in Figure 3.11c are compared to those in Figures 3.1b and 3.2a. The action of Δe_r is to slightly increase e_s values as the appearance of capillary waves increases in locations with higher wind. Foam emissivity, e_f, is calculated with (3.18-3.20). Figure 3.11d shows high values for e_f, from 0.913 to 0.942. Though the range of values shifts

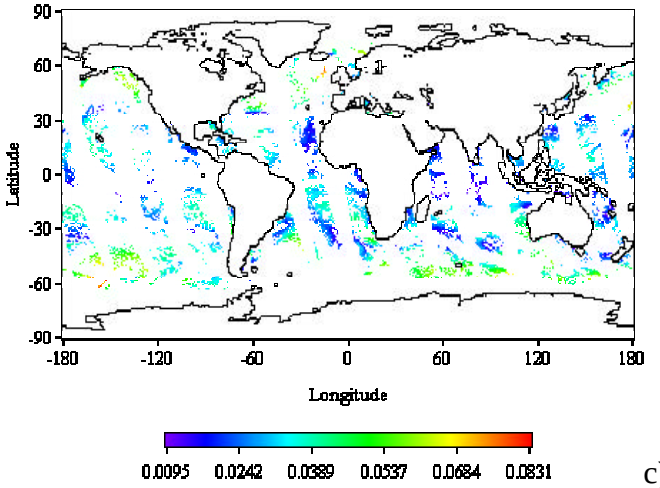

c)

Rough-sea emissivity, Δe_r

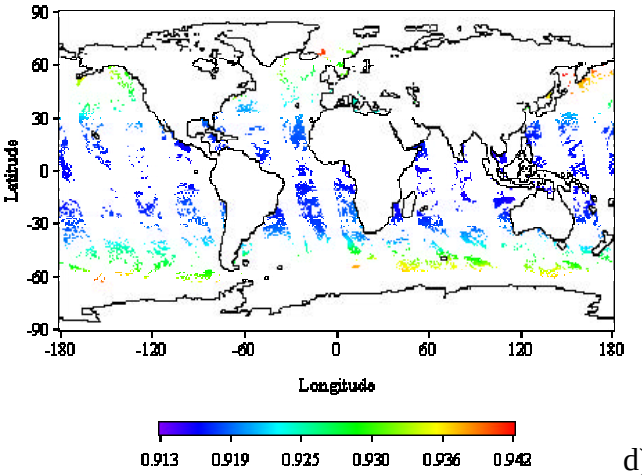

d)

Foam emissivity, e_f

Figure 3.11 Rough-sea emissivity, Δe_r (c), and foam emissivity, e_f (d) for 27 March (Julian day 86), 1998; maps 0.5 °×0.5 °.

close to unity, the patterns in the e_f map conspicuously follow those of T_s in inverse fashion, as was the case with the e_s values.

3.3.2 Whitecap coverage

Analytical investigation

The discussion of the crossing point between e and e_s (Figures 3.9) hints that certain atmospheric conditions would restrict a reliable estimation of W. When e values are too low, (3.2) would yield physically meaningless negative values for W. For instance, W cannot be determined in cases coupling high humidity with low whitecapping under low winds. Ranges of valid estimation of W at different humidities are shown in Figure 3.12. Under dry conditions (e.g., V = 8 mm), the entire range of possible T_B values (from about 105 to about 175 K) can be used to obtain valid estimation of W. As humidity increases (e.g., V = 20, 35, 50 mm), critical T_B values appear (marked in Figure 3.12 with vertical lines) at which W becomes 0. Values of T_B *above* these critical points would yield valid estimation of W, while T_B values below the critical points would produce negative meaningless W estimates. Thus, the effect of the atmosphere is in narrowing the range of satellite measurements useful for retrieving valid W estimation.

As mentioned earlier, Pandey and Kakar (1982) also encountered negative values for W in their microwave emissivity model. Indeed, the performance of their model is most likely plagued by two issues: i) Stogryn's expression underestimates foam emissivity (recall § *Foam emissivity* e_f); ii) they use T_B data from the Scanning Multichannel Microwave Radiometer (SMMR), which is known to have problems (Wentz and Francis, 1992). In addition, however, there are unavoidable physical restrictions for remote estimation of W, as the analysis in this study shows, and, I believe,

these restrictions have surfaced in Pandey and Kakar's model too. They rectified the problem by subtracting a constant bias from Hollinger's expression for roughness emissivity and adding a constant bias to the Stogryn's (1972) expression for foam emissivity.

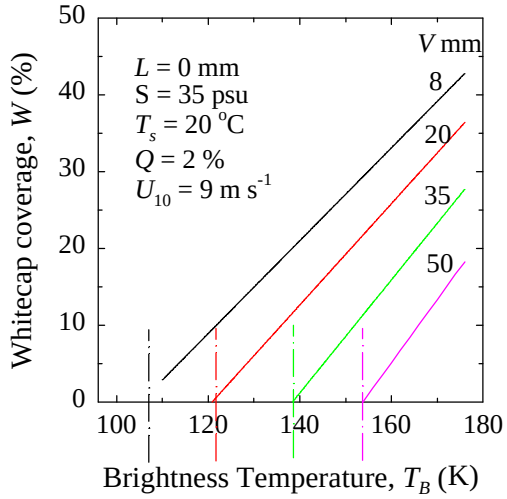

Figure 3.12 Values of brightness temperature, T_B, above critical points (marked with vertical lines) for different atmospheric humidity, V, yield valid estimates of whitecap coverage, W.

Observations

The approach of the current study to the problem of retrieving negative W is to discard all pixels for which $W < 0$; these are obviously erroneous estimations. For the day under consideration (27 March, 1998), the number of unrealistic negative W values is 335, about 2.1% of all estimated W-values. For any other day of 1998, the number of such estimates ranges from 2% to 10% of all estimated Ws. Thus, the conditions

constraining the estimation of *W* would not affect the number of *W* entries in the *W* database noticeably.

Whitecap coverage *W* for 27 March 1998 is given in Figure 3.13a. The range of *W* is from less than 1% to about 24%; in the figure, the *W* scale is given as a

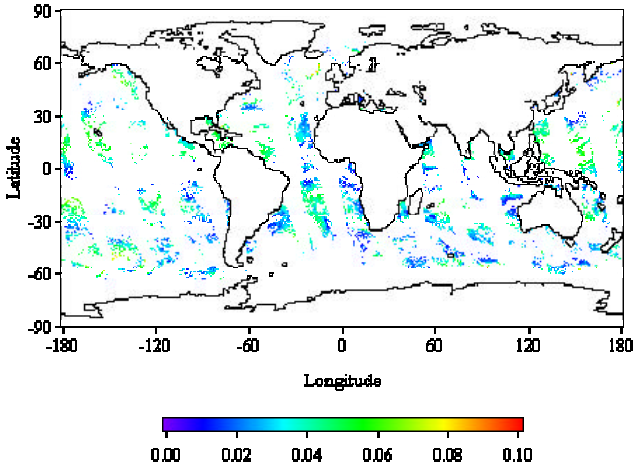

a)

Whitecap coverage, *W*

b)

Whitecap coverage, *W*

Figure 3.13 Result of new method estimation for 12 March (Julian day 86), 1998; map 0.5°×0.5°: a) Whitecap coverage, *W*; Distribution of *W*-values.

fraction, not a percentage, and is stretched over the 0-0.1 range to reveal global patterns well. As Figure 3.13b depicts, most *W*-values (97% of all estimated values) are in the range of 0.6% to 6%.

Retrieving *W* at several different values of the void fraction a investigates the effect of the void fraction choice. In Figure 3.14 the distributions and averaged *W* at a = 99%, 95%, 85% and 60% are compared with those obtained with a = 98% (equivalent to *Q* = 2%). The trend is: with a decreasing, the averaged *W* increases and the distributions become wider, featuring more high *W* values. The reason is that the lower a (i.e., the more water, *Q*, the foam contains), the lower foam emissivity, e_f,

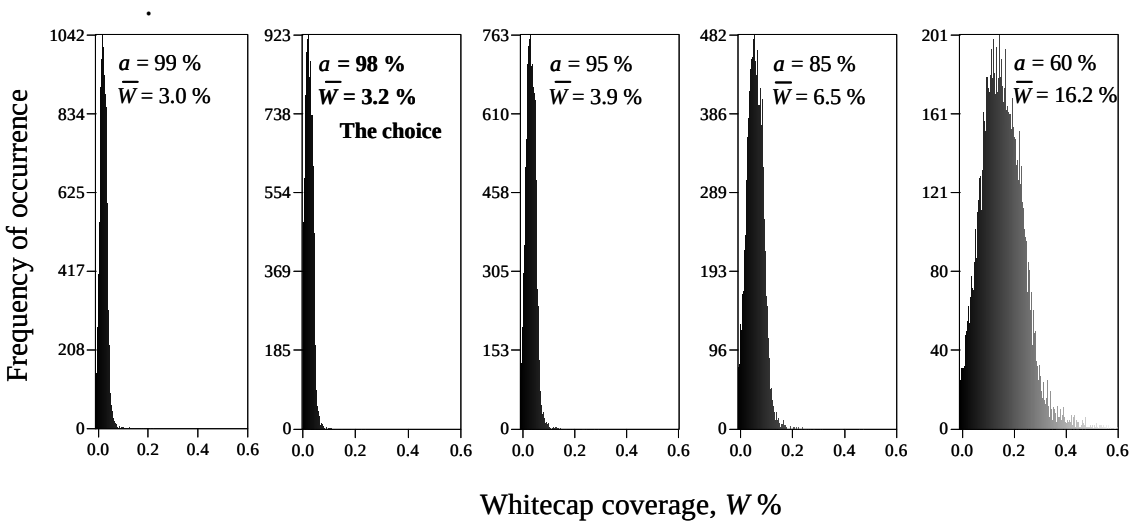

Figure 3.14 Comparison of the *W*-value distributions at different void fractions a.

until eventually it approaches the value of e_s. With e_f lower, (3.2) gives higher *W*. For any a in the range of 95-99%, the distributions do not change significantly, and the averaged *W* differ at most 23%. As a approaches 85%, the border of dry and wet foam,

W values are still realistic, but the average W is a bit higher than the previous *in situ* estimates. At a = 60%, W achieves unrealistically high values, including > 1. In conclusion, the choice of a = 98%, which is almost in the middle of the range giving the most reasonable W values, seems appropriate. The possibility of choosing a arbitrarily in the range 95-99% could be taken into account in the error analysis with the choice of the standard deviation of the void fraction, e.g., s_Q = 4-5%.

3.3.3 Errors

Analytical investigation

Figure 3.15 shows the sensitivity coefficients entering (3.26). According to (3.26), these sensitivity coefficients measure the error contributions of nine variables (T_B, V, U_{10}, T_s, S, $e_¥$, s, q, or Q) and some of their co-variations to the errors of the emissivities e, e_s, Δe_r, and e_f. After considering the figure, several conclusions emerge. The error of the incident angle, q, has a noticeable influence for all emissivities as the relatively high values of the sensitivity coefficients and covariant terms involving q show (see E_{eq} and E_{Vq} in panel a, E_{sq} in panel b, E_{rq} in panel c, and E_{fq} in panel d). The contribution of the error of S is the least (E_{sS} in panel b, and E_{fS} in panel d). The error of T_s is not of great importance for e and Δe_r as the low values of E_{eT} in panel a and E_{rT} in panel c show. However, the contribution of the T_s error changes significantly over the T_s range for e_s and e_f (see E_{sT} in panel b and E_{fT} in panel d). Coefficient E_{rU} in panel c has the highest values showing that the most significant contribution to the error of rough-sea emissivity comes from the error in measuring the wind speed, U_{10}. The variance of the water fraction, Q, contributes most to the error of foam emissivity (coefficient E_{fQ} in panel d). Though not large, the contributions of the error of s and $e_¥$

to the errors of e_s and e_f are tangible (see E_{ss} and $E_{s¥}$ in panel b, and E_{fs} and $E_{f¥}$ in panel d).

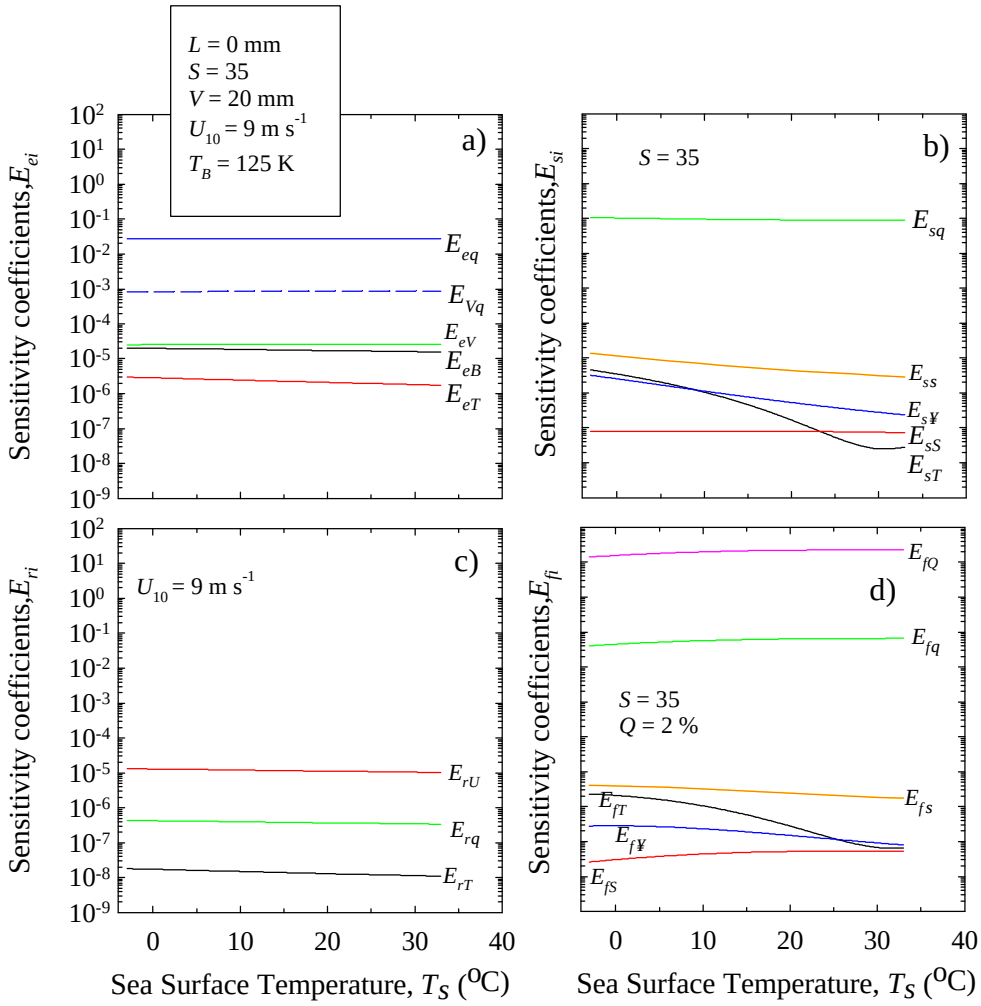

Figure 3.15 Sensitivity coefficients entering (3.26) as a function of T_s: a) E_{ei} for seawater emissivity, e; b) E_{si} for specular emissivity, e_s; c) E_{ri} for emissivity of rough sea, Δe_r; d) E_{fi} for foam emissivity, e_f. The index i has different notations showing the variable involved in the errors of the emissivities.

The propagation of error for the whitecap coverage is shown in Figure 3.16. The figure displays graphs of the sensitivity coefficients and their respective variances and co-variance in (3.23) as functions of T_s (panels a and b) and V (panels c and d). As panel a shows, errors in estimating e, e_s, and Δe_r would contribute most to the error of W, since their sensitivity coefficients (W_e, W_s, and W_r, respectively) are largest (black, red, and green lines). The variances of these emissivities, however, are

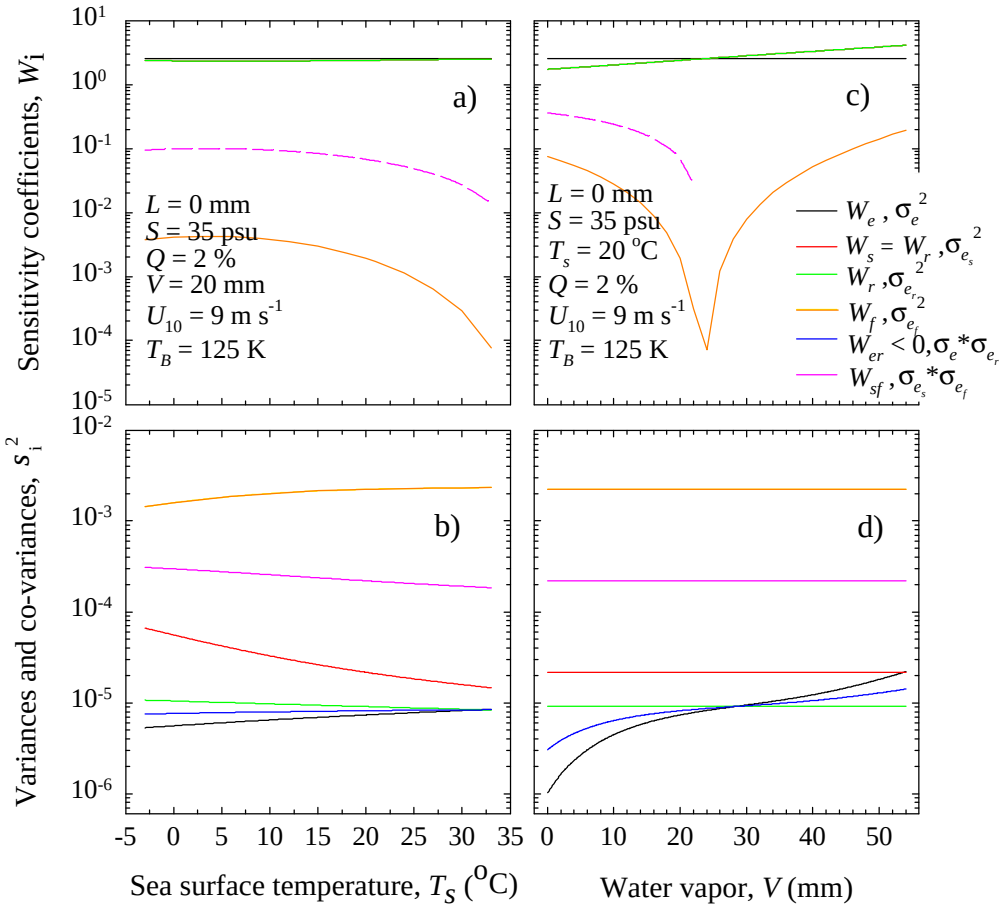

Figure 3.16 Sensitivity coefficients and their respective variances for W as a function of T_s (panels a and b), and as a function of V (panels c and d).

low (panel b), which neutralizes their potentially substantial contribution. Meanwhile, the lowest sensitivity coefficient W_f (orange lines in panels a and c) is coupled with the highest variance of the foam emissivity, $s^2_{e_f}$ (orange lines in panels b and d). The effects of the two co-variant terms are opposite: while W_{sf} adds to the error (pink line), W_{er} with its negative sign diminishes it (blue line, not seen in the figure). The plots versus V in panels c and d reveal that at the points where the evaluation of W is restricted due to the effect of atmospheric humidity (for the concrete case in the figure at V = 24 mm), the behavior of the sensitivity coefficients and their variances changes. This implies that the error of W at these points will also change drastically.

Figure 3.17 confirms such an expectation. The figure plots the relative error of W (= s_W/W) in % as a function of T_B for several values of V (8, 20, 35 and 50 mm) with solid lines and values along the left axis. The graphs $W(T_B)$ from Figure 3.12 are repeated here with dotted lines and values along the right axis in order to show the positions on the T_B axis of the points beyond which a meaningful estimation of W is possible. As $W(T_B)$ lines approach these limiting points, marked with vertical dash-dotted lines for each V value, the relative error of estimating W increases. Note that the higher the humidity, the larger the error. For dry atmosphere (V = 8 mm), W could be estimated from all measured T_B values with a relative error as low as 9% and as large as 33%. For wet conditions (V = 50 mm), the error is below 20% only for very high T_B values, and, approaching the limiting point at around T_B = 152 K, increases up to 80%.

Figure 3.18 summarizes the relative error of estimating W over the range of observable T_B, T_s, V, and U_{10}. The relative error varies from 8% to more than 400% for all possible environmental conditions. High whitecapping (W > 5%) could be estimated

confidently with a relative error less than 20%. For low *W* values, however, the error increases and could become extremely large.

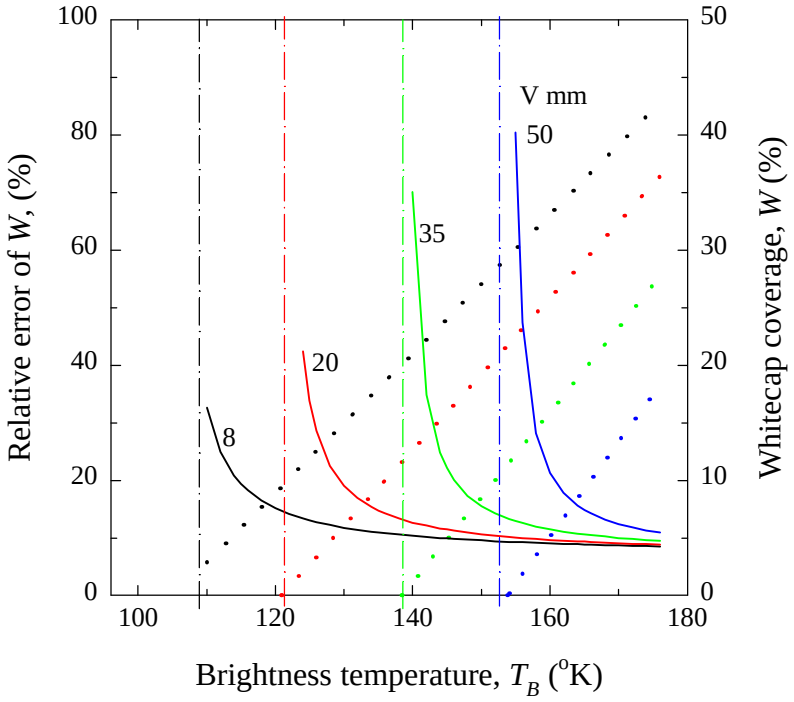

Figure 3.17 Relative error of whitecap coverage, *W*, as a function of brightness temperature, T_B, at various water vapor, *V*, (solid lines and left axis). Values of *W* for each error curve are also plotted (dotted lines and right axis). Water vapor determines the point above which T_B values can be used to estimate *W* (vertical lines).

Observations

The new method computes a map of standard deviation, s_W, for each daily map of *W*. A relative error for each estimated *W*-value is thus available. The relative errors of estimating *W* for 27 March 1998 vary widely, from 9% to more than 6,000%.

As anticipated from the analytical investigation of the error, this is not a surprising result. Any new algorithm encounters conditions in which the error approaches infinity, making the calculations or measurements inapplicable under certain conditions (Blanc, 1987; Andreas, 1991).

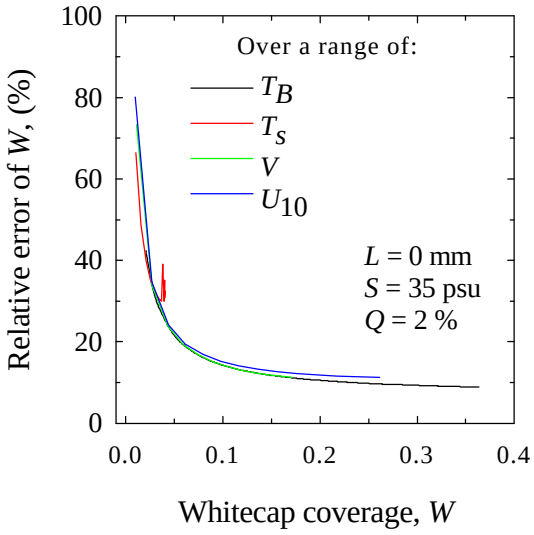

Figure 3.18 Relative error for estimating whitecap coverage, *W*.

The question then is: What is the acceptable error for *W* estimation? Let's make an arbitrary choice and announce a relative error of 30% as a criterion for a reliable estimation of *W*. Applying this criterion to the retrieved *W*s deems only 48% of all retrieved *W*-values as acceptable, and discards the remaining *W*-values as "bad" data. Moreover, with no exception, all discarded *W* estimates are for low whitecapping, which certainly creates a bias toward higher values in the distribution of *W*. Thus, there is a trade-off as to the tolerable error of the retrieved *W*-values, which must meet two

opposing requirements—keep the error as low as possible, yet not discard a statistically significant amount of data featuring low *W*.

A yardstick for judging the uncertainty in the new method of estimating *W* can be the uncertainty with which *in situ* measurements have previously obtained *W*. Ranges of relative errors for various experiments are listed in column 4 of Table 2.1: the photographic approach has estimated *W* values with uncertainty as good as 6% and as bad as 650%. The statistics show that one third of the *in situ* measurements have a relative error above 100%; about 44% of the measured *W*-values have a relative error from 30% to 100%; and 27% of all *in situ* values have an error below 30%. Monahan and O'Muircheartaigh (1980) used this type of data to extract the widely used empirical expression (2.3).

These facts point out that I can afford to increase the upper limit of the relative error of *W*, which would allow me to keep low *W* values. On the other hand, the number of retrieved *W*-values is so large (in order of 15,000 per day), that I can also afford to discard the *W*-values with error above 100% and with that improve the uncertainty of satellite-measured *W* compared to that of *in situ*-measured *W*. Thus, this study uses all *W*-values with a relative error up to 100%, and discards all *W*-values with an error above 100%. With this decision, the standard deviation of each retrieved value can be less or at most the value itself, i.e., $s_W \leq W$.

Applying this criterion to the *W*s retrieved for 27 March 1998 leads to the following statistics: 1) only about 5% of all retrieved data is "bad" data with an error above 100%; 2) about 47% of the retrieved *W*s have an error from 30% to 100%; and 3) about 48% of the *W*s have error below 30%. Two points are noteworthy: i) Indeed, the 5% "bad" data *all* comprise low *W* values, but this does not introduce statistically

significant changes in the *W* distributions; ii) The new method provides many more *W* data (about half of the estimates) with an error smaller than 30% compared to the *in situ* measured *W* (only about 1/3 of the measurements). Figure 3.19 shows the distribution of the relative errors of *W*-values retrieved for 27 March 1998. Error statistics of the satellite-measured *W* for all days in 1998 is similar.

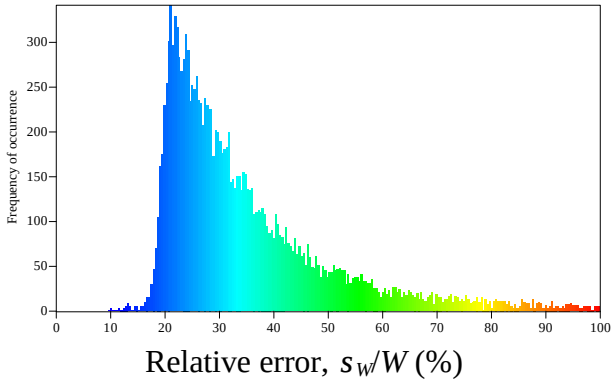

Figure 3.19 Distribution of the relative error of whitecap coverage for 27 March 1998.

3.4 Method validation

To validate the results obtained with the new method, it is necessary to compare the *W*-values derived with this method with *W*-values measured *in situ* or calculated differently. Despite the mismatch between spatial resolutions of satellite and *in situ* measurements, such a comparison is necessary in order to check, at least roughly, the validity of the new method and establish the new features, which this method introduces. Three approaches, described in this section, could be employed to validate *W* obtained with the new method.

3.4.1 Comparison with previous *in situ* data

Assuming that climatologically whitecap coverage is stationary, a comparison of W from satellite measurements with previous *in situ* measurements is straightforward. Of course, such a comparison is not the best validation approach, since local conditions could be quite different due to differences in time and location. Still, such a validation can provide an order-of-magnitude reference.

All compiled previous *in situ* data for W (Table 2.1 and Figure 2.3) are compared with W obtained from satellite measurements for 27 March 1998 in Figure 3.20. The new method estimates of W with relative errors up to 650% are also included to match the *in situ* data with similar errors. The first observation in Figure 3.20 is that both *in situ* and satellite measured W-values are of the same order of magnitude. Considering disparities such as spatial resolution, differences in local conditions, and differences in the measuring principles (photographic versus satellite measurements), the whitecap coverage estimated with the two methods are consistent.

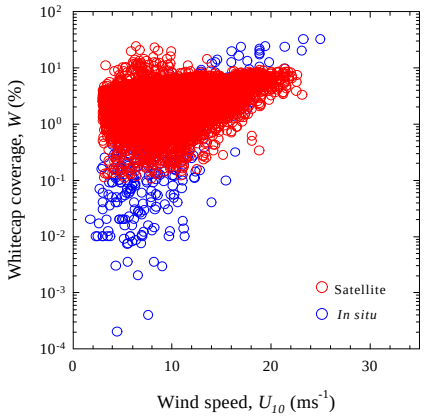

Figure 3.20 Comparison of *in situ*-measured whitecap coverage, W (data sets in Table 2.1), with satellite-measured W for 27 March 1998.

An interesting observation in Figure 3.20 is the difference in the trends of *in situ* and satellite-measured *W*. While *in situ W* exhibits a clear increase with increasing wind speed, *W* from satellite changes more slowly, i.e., the increasing trend is somewhat suppressed under high winds, whereas the *W*-values are higher and more variable under low to moderate winds.

Figure 3.21 shows *in situ W* measurements from individual experiments (Table 2.1) compared to co-located new-method estimates of *W*. There are several interesting observations in this figure. First, the three panels at the top of the figure all depict aerial measurements. They are systematically higher than the satellite-derived *W* estimates. Possible reasons are either inadequate correction of the effect of the atmospheric layer below the aircraft, or problems with the sensor calibrations. These issues are briefly, if at all, discussed in the respective papers. Next, the measurements reported by Bortkovskii (1987, missions Typhoon, *RV* Bugaev, and POLEX_YUG) compare with the new method estimates most favorably. Figure 2.2 shows that all these missions provide data for open ocean. The *in situ* measurements in the cold water also agree well with satellite-measured *W*, namely measurements in the Southern Ocean (Borthkovskii, 1983) and Gulf of Alaska (STREX ’80, Doyle, 1984) as Figure 2.2 points out. Finally, though generally consistent, data reported by Monahan and co-workers (BOMEX ’68, JASIN ’78, MIZEX ’83, MIZEX ’84) are usually much lower (factor of 10 to 100) than the new-method estimates. These are measurements in the North Atlantic and off Barbados (Table 2.1), locations with quite different environmental conditions, yet their comparison to the satellite *W* estimates is similar. Thus, a reason for systematically lower estimates by Monahan and his colleagues is probably due to the way they determine whitecaps on their photographs.

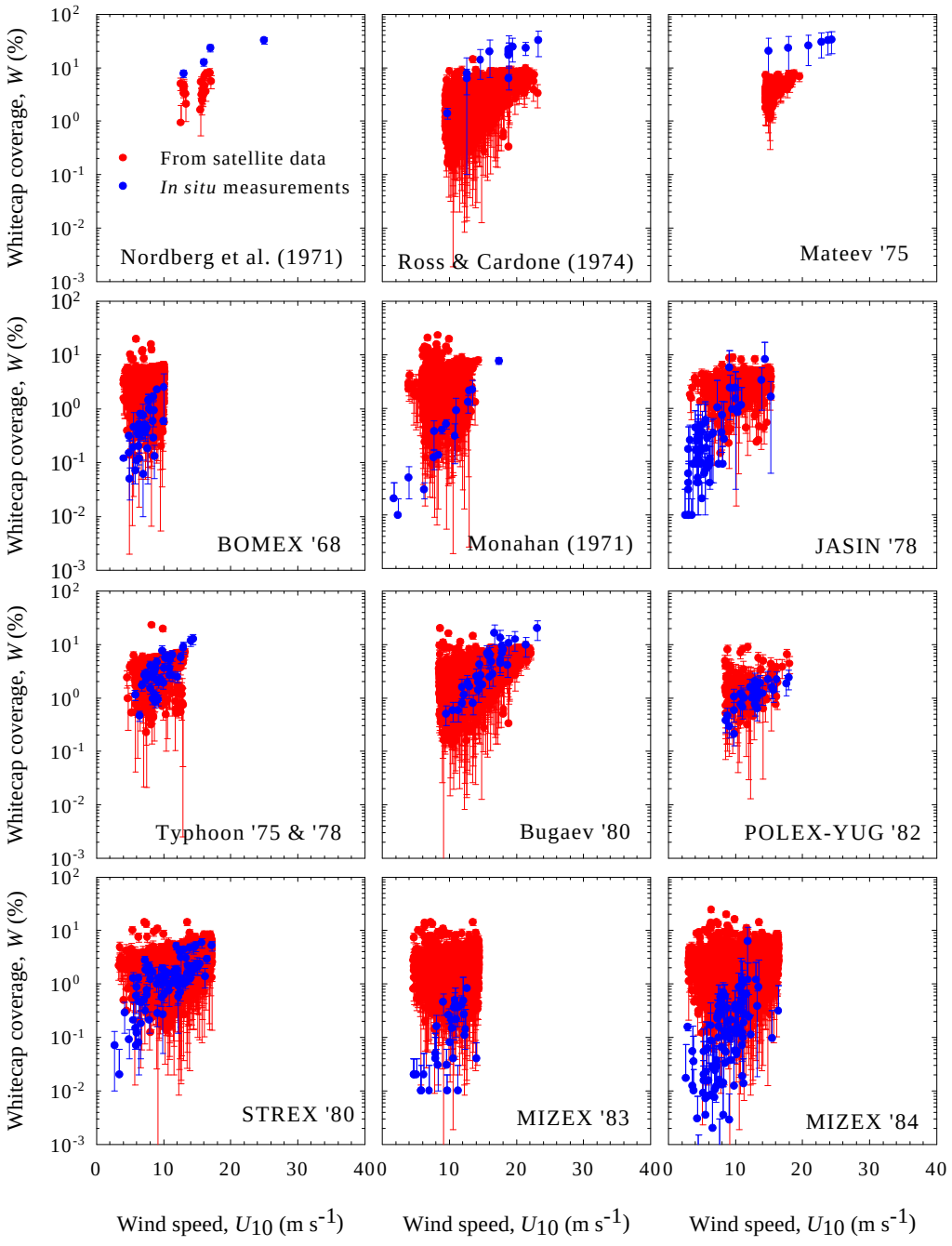

Figure 3.21 Comparison of individual *in situ* measurements of whitecap coverage with collocated new-method estimates for 1998.

Since they measure B-stage whitecaps only (Monahan, 1993), they probably underestimate *W*. Meanwhile, the new method is capable of detecting both A and B-stage whitecaps (recall *Void fraction choice*).

3.4.2 Comparison with the wind formula

There are several formulae proposed in the literature for estimating whitecap coverage from measured wind. Blanchard (1963) first established a relation between W and U_{10}. He used 5 aerial photographs of the sea surface taken from an aircraft in the Caribbean area and obtained a quadratic dependence of W on U_{10}, that is $W \propto U_{10}^{2}$. Stogryn (1972), cited by Tang (1974), used four data sets and best least-square curve fit to obtain $W \propto U_{10}^{3.231}$. Wu (1979) obtained $W \propto U_{10}^{3.75}$ applying least-square curve fitting to two data sets in warm waters, namely BOMEX (Monahan, 1971) and East China Sea (Toba and Chaen, 1973) (Table 2.1). Using the same data sets, Monahan and O'Muirchaetaigh (1980) proposed $W \propto U_{10}^{3.52}$ employing ordinary least-square analysis, and $W \propto U_{10}^{3.41}$ with robust biweigh fit analysis. Bortkovskii (1987) analyzed several data sets in warm and cold waters (Typhoon-75, Typhoon-78, POLEX YUG, see Table 2.1) and first reported different $W(U_{10})$ dependencies for different water temperatures:

$$W\,(\%) = 6.78\text{x}10^{-3}\, U_{10}^{\,2.76} \quad , 15 < T_s < 28\ ^{o}\text{C}$$

$$W\,(\%) = 1.71\text{x}10^{-5}\, U_{10}^{\,4.43} \quad , 3 < T_s < 15\ ^{o}\text{C}$$

$$W\,(\%) = 0.189\, U_{10} - 1.28 \quad , \qquad T_s < 3\ ^{o}\text{C}$$

Finally, Spillane et al. (1986) used STREX, JASIN, BOMEX, and the East China Sea data of Toba and Chaen (Table 2.1) to propose three different $W(U_{10})$ relations for cold, moderate and warm waters.

All published formulae represent $W(U_{10})$ as a power law. The only exception is Bortkovskii's linear dependence of W on U_{10} in cold waters. The power

laws listed above differ in their exponents and coefficients. Although values change due to differences in the exponents, maps of W produced with any of these formulae have similar features. Because the relation $W \propto U_{10}^{3.41}$ given with (2.3) became widely used in climate models, W-values computed with the new method are compared only with W-values computed with (2.3).

A map of global whitecap coverage computed with (2.3) from the wind field for 27 March 1998 is displayed in Figure 3.22. The composite mask for the day, used in the new-method calculations, was applied to the initial wind field for better

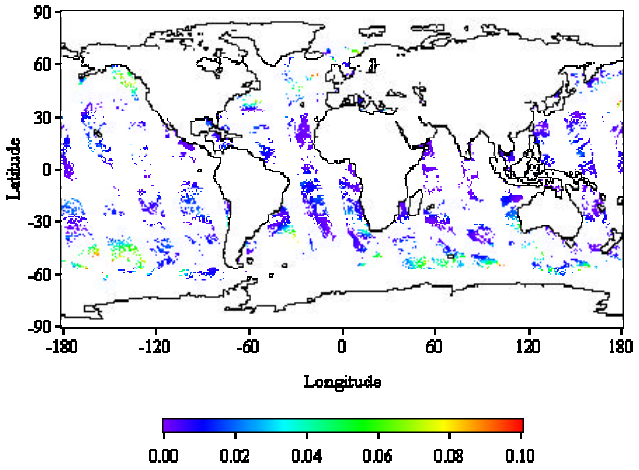

Figure 3.22 Whitecap coverage, *W*, calculated with wind speed formula (2.3) from the wind field for 27 March, 1998.

comparison between the two computations. The scale of W is stretched to show well the W-range up to 10%. W-values calculated with both methods are of the same order of magnitude: the wind formula yields W from less than1% to 17%, which is comparable with the range of < 1% to 24% from the new method.

Comparing Figure 3.22 with Figure 3.13a, however, reveals a substantial difference in the global distribution of *W*. Calculations with the wind-speed formula give high *W* mostly in high latitudes, while the new method gives lower *W*-values in high latitudes, and higher *W* in mid to low latitudes. It is argued here that the most probable reason for this difference is that the new method accounts well for the effects of environmental variables in addition to wind speed, namely sea surface temperature, salinity, and so on (for details see §4.2.2).

3.4.3 Comparison with matching *in situ* data

The best way of validating the new method is to compare *in situ*-measured *W* with satellite-derived or *in situ W* values for same times and locations. The only reason for differences between *in situ* and satellite *W* expected in these cases is the mismatch in the spatial resolutions. Two possibilities for time and space co-located comparisons emerged: SMMR data and GASEX'98 data.

The Scanning Multichannel Microwave Radiometer (SMMR), flown on NASA's Nimbus-7 satellite, provided routine measurements of brightness temperature of the ocean from October 1978 to August 1987. The new method for estimating *W* can be applied to SMMR $T_B(h)$ at 18 GHz for times and locations coinciding with those of the *in situ* datasets collected after 1978 (Table 2.1). The first attempt at validation of the new method with matching *in situ* data used whitecap coverage measured during MIZEX83 and MIZEX84 since Monahan's datasets of *W* are more complete. The daytime SMMR passes (the ascending passes) were used as most of the *in situ* measurements were done during the day. Very few cells (about 10 in each case) with available T_B from SMMR were found to match *in situ* data for the same day and location. The scarcity of matching *in situ*-satellite pairs of *W* can be explained with the

overall fewer T_B entries from the SMMR, which transmitted data every other day. The calculation of W with the new method used U_{10} and T_s values reported for each *in situ* W-value, and average S and V typical for the location. The comparison was disappointing—the satellite-derived W-values were consistently two orders of magnitude higher than the *in situ* W-values.

An inquiry revealed that the most probable reason for the failure of this validation is the use of daytime SMMR T_B. It became clear that SMMR brightness temperatures are plagued with problems due to an inadequate on-board calibration system (Francis, 1987). Use of SMMR data is possible only after performing corrections for the acquisition of the sun in the cold reference horn and changes in the sensor's temperature. Such corrections were successfully implemented for only three of the 10 SMMR channels (18 GHz not among them) and for the nighttime passes (Wentz and Francis, 1992). The practicality of doing these corrections for the daytime passes, when sun glint from the ocean surface adds to the problems, needs consideration. These findings made the calculation of W from SMMR T_B for other matching *in situ* measurements a nuisance. In short, there are not satellite-measured T_B suitable for estimating W and validating it with *in situ* data from Table 2.1. More recent *in situ* datasets need to be found in order to perform temporally and spatially matching validations of the new method.

Measurements of whitecap coverage were conducted during the Gas Exchange Experiment 98 (Gas Ex-98) in the North Atlantic (unpublished data by William Asher). Whitecap coverage was determined hourly with a photographic method for five days in June 1998 (Julian days 155, 158, 159, 160, and 163). The area covered with the ship for these five days is around 47 km $\times$ 50 km, which is commensurate with

one pixel (55.6 km×55.6 km) in the maps presented in this study. The water temperature and salinity were approximately constant during all measurements, namely T_s = 15.45 °C and S = 35.63 psu. These values are consistent with the T_s and S values used in the new method calculations for this location. Matching satellite and *in situ* W estimates were found for two days (159 and 163). The Gas Ex-98 daily averages of W are 1.14% and 0.3%. The corresponding satellite-derived W values are 4% and 3.4%. A possible reason for higher new-method estimates is that W values from Gas Ex-98 reflect mostly the A-stage of the whitecaps because the active bright areas are more easily and accurately spotted and evaluated from photographs than the dim areas of decaying whitecaps (Asher, 2002, personal communication). But A-stage whitecaps cover considerably less area. The ratios of areas covered by both stages of the whitecaps, W_A and W_B, range from W_B/W_A = 2.86 to 18.2 (Monahan, 1989). If Gas Ex-98 values represent mostly W_A, they need to be corrected to include W_B in order to fairly compare them with the satellite-derived W. Choosing W_B/W_A = 3 (the lower limit of the ratio), the values from Gas Ex-98 become $W_A + W_B = W_A + 3W_A$ = 4.56% and 1.2%.

3.5 Summary and possible improvements

The method proposed in this study for estimating W from satellite-measured brightness temperature of the ocean surface works well, especially for moderate to high wind speeds. It provides daily whitecap coverage on a global scale. The new method improves the accuracy of predicting whitecap coverage. The satellite-derived retrievals of global W have a relative error below 100% in 95% of all estimates, while *in situ* photographic measurements provide W with an error below 100% in 71% of all measurements.

This first version of the new method can be further improved. The main lines of improvement are modeling the dielectric constant of seawater, understanding more about the foam emissivity, and performing a more accurate atmospheric correction.

As Figure 3.15 shows (panels b and d), errors in seawater conductivity, σ, and dielectric constant at infinite frequency, ε_∞, introduce non-negligible errors into the computation of specular and foam emissivities. Better accuracy of σ and ε_∞ will, therefore, improve the estimation of W.

In this initial version of the new method, the calculation of ε'' in (3.14) uses a constant value for seawater conductivity, $\sigma = 5.32\ \Omega^{-1}\ m^{-1}$. The conductivity of seawater, however, depends strongly on sea surface temperature, somewhat less strongly on salinity, and very weakly on pressure. Thus, expressions for $\sigma(T_s, S)$ have to be found and included in the calculations.

From experiments in the early 1950s, ε_∞ is known as a constant with a relative error of ± 20% (Klein and Swift, 1977). Thorough investigations, however, show that ε_∞ changes with temperature and frequency (Hasted, 1973). Guillou et al. (1998) report new precise measurements between 3 and 20 GHz documenting values of ε_∞ from 6 to 9, depending on the temperature. An updated value of ε_∞ as a function of T_s should be incorporated into the W estimation.

The empirical expressions for ε_s and τ, given by Klein and Swift (1977) and used in the first version of the new method for W estimation, have also been questioned (Guillou et al., 1998). A search in the literature for new experiments and analyses resulting in improved parameterization of ε_s and τ and their inclusion in the estimation of W is recommended.

Literature review or experiments furthering the general understanding of foam emissivity, especially its dependence on changes in foam thickness, can be helpful to obtain a more appropriate choice of the water fraction, Q, in the whitecaps.

The atmospheric correction could be improved in two ways. First, the reflected downwelling radiation should be modeled better. Currently, the term $(1 - e)tT_{BD}$ in (3.3) describes specularly reflected downwelling radiation, i.e., sky radiation coming into SSM/I from an angle equal to the incident angle q. For a rough sea surface, however, sky radiation, reflected into the direction of SSM/I from surface facets tilted in various directions, will add to this term. This additional sky radiation could be accounted for with a factor involving the sea surface slope variance, which, in turn, depends on wind speed (Wentz, 1997). Second, the seawater emissivity, e, should be modeled better. Bursting bubbles within whitecaps create a layer of droplets above the sea-surface interface. Seawater droplets make this layer more absorptive compared to a layer with air only, which changes the brightness temperature of the ocean surface. The effect of this transition zone from the ocean to the air on the seawater emissivity can be accounted for with an additional term included in the RTE (3.3). An algorithm, proposed by Tang (1974), can be used to evaluate the effect of droplets on T_B at 19 GHz. If the effect of droplets is significant in magnitude, it should be introduced in the calculation of seawater emissivity, e.